Primary and secondary nonlinear global instability

A. Couairon *, J.-M. Chomaz

Laboratoire d'Hydrodynamique, LadHyX, CNRS UMR 7646, École Polytechnique, F-91128 Palaiseau, France

Abstract

We study oscillating solutions of the complex Ginzburg–Landau equation in a semi-infinite domain asymptotic to a saturated traveling wave at $+\infty$ and subject to a homogeneous upstream boundary condition at $x = 0$. This inlet condition breaks the Galilean invariance, giving the advection velocity the role of a control parameter. We give a criterion for the existence of a nontrivial solution called a nonlinear global mode or a self sustained resonance, and we obtain the selected frequency. The threshold and the frequency are shown to be determined by the linear absolute instability transition. We undertake a singular perturbation analysis which first proves the validity of the criterion and secondly yields scaling laws for the frequency, the growth length and the slope at the origin of the nonlinear global modes as functions of the criticality parameter. Comparisons with direct numerical simulation of the Ginzburg–Landau model validate these predictions. Furthermore, the results are in excellent agreement with numerical simulation of the Taylor–Couette problem with throughflow by Büchel et al. [P. Büchel, M. Lücke, D. Roth, R. Schmitz, Pattern selection in the absolutely unstable regime as a nonlinear eigenvalue problem: Taylor vortices in axial flow, Phys. Rev. E 53 (1996) 4764–4777] and of Rayleigh–Bénard flow with an added Poiseuille flow by Müller et al. [H.W. Müller, M. Lücke, M. Kamps, Convective patterns in horizontal flow, Europhys. Lett. 10 (1989) 451–456; H.W. Müller, M. Lücke, M. Kamps, Transversal convection patterns in horizontal shear flow, Phys. Rev. A 45 (1992) 3714–3726]. The numerical simulations indicate that the nonlinear global modes are stable if the saturated traveling wave to which the nonlinear global mode is asymptotic (i.e. the asymptotic downstream part of the global modes) is not absolutely unstable to perturbations. A complete analysis of the dispersion relation of the secondary instability of saturated traveling waves is given.

1. Introduction

It is often put forward that a first step toward understanding complex dynamics in spatially extended nonequilibrium systems is to find solutions describing a basic pattern which plays a crucial role in the long time behaviour (such as pulses, fronts, holes [1]). The goal of the present paper is to describe a class of such solutions, called

---

* Corresponding author. E-mail: couairon@cpht.polytechnique.fr.

nonlinear global (NG) modes [2–5], which are believed to account for the dynamics of open flows. In open flows, fluid continuously enters and leaves the domain of study and, as a result, instability waves are in general advected by the mean flow. An NG mode may be viewed as a solution able to withstand the advection. It oscillates at a characteristic frequency in the whole domain and constitutes a good candidate to describe self sustained oscillators that are observed in wakes [6–10], Taylor–Couette flow with throughflow [5,11] or Rayleigh–Bénard convection with an added Poiseuille flow [12,13]. In astrophysics, a dynamo model of magnetic field generation in the sun, leading to NG mode solutions has recently been proposed [14].

In closed extended systems, particular solutions describing a basic pattern are the 'coherent structures' [1] which are localized states or consist of domains with regular patterns separated by interfaces. For example in one-dimensional systems, these interfaces may be fronts, pulses, or holes [1,15]. Experimentally, fronts have been observed in various systems as binary fluid mixtures [16], Taylor–Couette flow between rotating cylinders [17] and chemical reactions [18]. Pulses are used in nonlinear optics to propagate light wave in fibers [19,20] and holes, or localized defects, have been shown to play an important role in spatio-temporal intermittency [21–24]. More precisely, each propagating coherent structure (pulse, front, hole) observed in an infinite geometry moves at a specific velocity with a specific frequency. In this case, the problem to be solved is the selection of a single structure among a continuous family, as the long time asymptotic solution of the system. In Taylor–Couette flow between rotating cylinders [17], when the control parameter (the Taylor number) measuring the rotation velocity of the inner cylinder is abruptly increased above a critical threshold, a vortex front establishes itself and propagates away from the boundary, leaving toroidal rolls in the bulk of the domain, with a wavelength which is selected by this very front structure, and is independent of initial conditions or parameter history. The same phenomenon occurs in the Rayleigh–Bénard [25] system when the temperature difference across the cell (the Rayleigh number) is abruptly increased above threshold, a convective vortex front moves into the unstable conductive state. To describe these structures, Ginzburg–Landau type models are extensively used as they constitute the simplest models one could construct that combine instability, diffusion, advection of perturbations downstream, and nonlinearity. In addition, these models are able to exhibit an incredibly large spectrum of dynamical behaviour varying a few parameters. Ginzburg–Landau equations with real coefficients were first derived by Newell and Whitehead [26] and by Segel [27] as long wave amplitude equations for convection rolls in the Rayleigh–Bénard experiment, close to their instability threshold. Complex Ginzburg–Landau equations were derived by Stewartson and Stuart [28] who have studied plane Poiseuille flow.

When studying open flows, since a reference frame is usually singled out by the inlet and outlet conditions, upstream conditions and advection velocity must be considered explicitly. When the primary instability is two-dimensional (Squire's theorem for shear flows), the leading spatio-temporal dynamics of open flows varying along the streamwise direction has been analyzed in a one-dimensional semi-infinite domain [2]. At the inlet, the amplitude of the perturbation vanishes since the basic flow is enforced there by the boundary condition $A(0) = 0$, which represents the ideal case of a medium with zero level noise at the entrance. This breaks Galilean invariance and introduces a new parameter in the system, the advection velocity, which turns out to severely limit the multiplicity of solutions observable in a semi-infinite domain. Although in the previously mentioned closed flow case, the translation velocity of a particular coherent structure is selected by some principle, the situation is different in the open flow case. This is because the mean advection velocity is a fixed parameter and only coherent structures that propagate at a velocity sufficient to withstand the advection, and that are able to accommodate the boundary condition can describe the pattern observed in a real experimental setup. (This should be easier if the amplitude of the coherent structure vanishes at some location in the infinite domain.) The problem of pattern selection in a semi-infinite domain with advection U_0 then possesses discrete solutions, since in a family of coherent structures valid in an infinite domain, only the structure propagating at a velocity exactly opposite to the advection will be a plausible steady or time-periodic state of the system, particularly if it also possesses a point of zero amplitude.

In the present study, we will illustrate these ideas by describing NG modes for the Ginzburg–Landau equation; the term 'NG' mode refers throughout this paper to a time-periodic solution of a one-dimensional system which links a state imposed by the upstream condition ($A(0) = 0$) and a finite amplitude state at infinity represented by a traveling wave. Intuitively, these NG modes may be viewed as fronts which have propagated upstream and stopped at the inlet boundary. The usual problem of velocity and frequency selection for the fronts is here advantageously replaced by a problem of existence of solutions, since the advection velocity is a fixed parameter and the frequency selection will naturally be derived from the existence criterion. In particular, we seek the threshold of existence of the NG modes, hereafter denoted the NG threshold, and we show that it may be determined by the now widely used concepts of linear absolute and convective instability [2]. The frequency selection mechanism, on the other hand, is found to be strongly nonlinear. Classically, transition to disorder is obtained by creation, competition and annihilation of coherent structures. But in an open system, the advection velocity has a strong regulating effect and above the primary bifurcation, NG modes represent the nonlinear spatial distribution of fluctuations. We address the question of stability of the NG modes and the secondary bifurcation is shown to coincide with the absolute threshold for the secondary instability, i.e. the absolute instability of the saturated traveling wave at infinity. This secondary bifurcation is somehow similar to what happens with holes in one dimension [29–31] or spirals in two dimensional systems [32]; both select a unique wavenumber 'far' from the singularity, which can be in the stable or in the unstable band. These successive bifurcations constitute a scenario for the transition to disorder in open systems.

The outline of this paper is as follows. In Section 2, we present the model and set out the existence problem. A phase space analysis allows us to solve this existence problem and in particular, to give a straightforward frequency selection criterion. In Section 3, a singular perturbation analysis near the NG threshold allows us to derive scaling laws for the frequency and the spatial growth length of the NG modes. These laws compare satisfactorily with numerical measurements for the Taylor–Couette problem with throughflow by Büchel et al. [11] and for the Rayleigh–Bénard flow with an added Poiseuille flow by Müller et al. [12,13]. In Section 4, some numerical simulations are presented and give an independent validation of the scaling laws, which is particularly useful in the region of parameter space 'far' from the real case where no comparisons with published work are available.

These temporal simulations allow us to determine the stability of an NG mode. We establish numerically that the region of parameter space where an NG mode may be observed depends on the stability of the asymptotic traveling wave. An NG mode will be unstable if its asymptotic traveling wave is absolutely unstable. This secondary absolute or convective instability is determined by the analysis of the dispersion relation of linear perturbation waves on the nonlinearly saturated basic traveling wave state. We propose these two successive bifurcations as the basis of a scenario for the transition to disorder in open systems. These two bifurcations may occur either sequentially or simultaneously if the absolute threshold for the secondary instability of the plane wave precedes the threshold for the primary bifurcation. For the latter case, the transition to disorder will occur suddenly through a single bifurcation.

2. The Ginzburg–Landau model

We consider the complex supercritical Ginzburg–Landau equation, which may be derived for example by a weakly nonlinear analysis of the Taylor–Couette system or Rayleigh–Bénard convection, with throughflow [11–13]. This derivation has been carried out by Büchel et al. [11] for the Taylor–Couette system and by Müller et al. [13] for Rayleigh–Bénard convection, and we will use the values they have obtained when comparing our results with a particular experiment. More generally, we will consider the Ginzburg–Landau equation as a prototype problem and explore its dynamics. The Ginzburg–Landau equation reads

$$\frac{\partial A}{\partial t} + U_0 \frac{\partial A}{\partial x} = (1 + ic_1)\frac{\partial^2 A}{\partial x^2} + \mu A - (1 - ic_3)|A|^2 A, \tag{1}$$

where U_0 denotes the advection velocity ($U_0 > 0$ by definition). A rescaling of A, x and t would allow to set to unity either U_0 or the bifurcation parameter μ but we will keep both parameters till Section 4 in order to facilitate comparison with experiments. The coefficients c_1 and c_3 are real and c_1 is assumed to be positive since Eq. (1) possesses the symmetry ($A \to \overline{A}, c_i \to -c_i$), where the overbar denotes complex conjugation.

For the evolution of infinitely small perturbations, we shall refer to the linear absolute instability theory initially developed in the context of plasma physics [33–35]. The laminar state $A = 0$ is said to be *convectively unstable* if disturbances propagate away from the localized initial source region and *absolutely unstable* if they spread upstream and downstream and contaminate the whole medium. In the present case, the nature of the linear instability of the uniform state $A_0 \equiv 0$ is defined by

$$\mu_A \equiv \frac{U_0^2}{4(1 + c_1^2)} \tag{2}$$

and the flow is linearly convectively unstable [2] for $0 < \mu < \mu_A$ and linearly absolutely unstable for $\mu > \mu_A$. The absolute frequency, the frequency which dominates the asymptotic solution at any fixed location, equals at threshold $\mu = \mu_A$:

$$\omega_A \equiv -c_1\mu_A = -\frac{c_1 U_0^2}{4(1 + c_1^2)}. \tag{3}$$

Of course, the distinction introduced above between absolute and convective instability makes sense only when the Galilean invariance is broken and a particular frame is singled out. This will be the case when a boundary condition is introduced at $x = 0$ to mimic the inlet condition of a real open flow. As we will show, the μ_A threshold will play a crucial role in the existence of a finite amplitude solution of Eq. (1). This solution is an NG mode, able to withstand the advection U_0 while also accommodating the boundary condition. This NG mode will be asymptotic to a traveling wave solution at infinity and we shall address the problem of existence, multiplicity and nature of the traveling wave solution before going any further.

Throughout the paper, we consider that the parameters U_0, c_1, c_3 are fixed and will describe the solutions in the (μ, ω) plane, ω being also considered as a parameter until we address the problem of its selection in some particular case. Because of the symmetry $A \to A e^{i\theta}$, we always describe the solutions of Eq. (1) up to an arbitrary phase.

2.1. Traveling waves

Eq. (1) exhibits [36] a family of saturated traveling waves solutions parametrized by ω:

$$A_2 \equiv a_N e^{iq_N x - i\omega t}, \tag{4}$$

where a_N, q_N and ω are real and obey

$$a_N^2 = \mu - q_N^2, \tag{5}$$

$$\omega = U_0 q_N + c_1 q_N^2 - c_3 a_N^2. \tag{6}$$

Equations (5) and (6) possess two solutions $q_N^\pm$, the dissymmetry between q_N^+ and q_N^- being due to the Doppler effect introduced by the advection which breaks the $x \to -x$ symmetry:

$$q_N^\pm = -\frac{U_0}{2(c_1 + c_3)} \pm \frac{1}{2(c_1 + c_3)}\sqrt{U_0^2 + 4(c_1 + c_3)(\omega + c_3\mu)}. \tag{7}$$

The condition that a_N^2 be positive Eq. (5) restricts the domain of existence of each solution. For fixed U_0, c_1, c_3, the region of existence of the solutions (a_N^+, q_N^+) in the plane (μ, ω) is bounded by the thick solid lines in Fig. 1
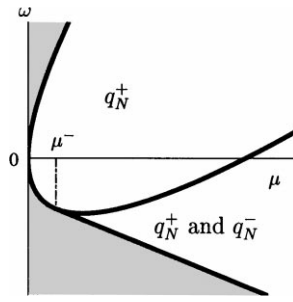
Fig. 1. Domain of existence of the traveling waves (a_N^+, q_N^+) and (a_N^-, q_N^-). In the gray region, no solution exists. Traveling wave (a_N^+, q_N^+) exists in both white regions, whereas (a_N^-, q_N^-) exists for $\mu > \mu^-$ in the lower white region only.

and corresponds to the white zone. Solutions (a_N^+, q_N^+) exist for $\mu > 0$. We represent the region of existence of the solutions (a_N^-, q_N^-) in the same manner but (a_N^-, q_N^-) only exists for $\mu > \mu^-$ in the lower white region, with

$$\mu^- \equiv \frac{U_0^2}{4(c_1 + c_3)^2}. \tag{8}$$

It should be emphasized that for $0 < \mu < \mu^-$, the system (5) and (6) possesses a single nonlinear solution (a_N^+, q_N^+). The question of the stability of the traveling waves will be addressed later.

2.2. NG modes

In a semi-infinite domain, NG modes are defined [37,38] as time-periodic solutions of Eq. (1), therefore satisfying:

$$-i\omega A = (1 + ic_1)\frac{d^2 A}{dx^2} - U_0\frac{dA}{dx} + \mu A - (1 - ic_3)|A|^2 A, \tag{9}$$

with the boundary condition at the origin $A(0) = 0$. At infinity, the NG mode is asymptotic to a traveling wave of type Eq. (4). For $\mu < \mu^-$, utmost a single traveling wave solution exists and there is no ambiguity. For $\mu > \mu^-$, two traveling waves with the same frequency exist but, as argued in [15] where fronts are considered, only the solution q_N^+ is physical since it corresponds to a positive 'nonlinear group velocity' $d\omega/dq_N$, allowing 'information' to be propagated in the downstream direction, whereas the q_N^- solution corresponds to a negative group velocity and propagates the 'information' upstream. Therefore, only (a_N^+, q_N^+) will be considered below and the plus sign is dropped for clarity.

To absorb the phase invariance $(A \to Ae^{i\theta})$, an NG mode may be written in the form

$$A(x, t) = a(x)e^{i\int^x q(x')\,dx'}e^{-i\omega t}, \tag{10}$$

with $a(x), q(x), \omega$ real. This transformation has been used for the study of front propagation in infinite domains [15,39–41] and associated with the singular change of variable $k = \dot{a}/a$, called the σ-process by Arnol'd [42].

Under the change of variable Eq. (10), the initially second-order Eq. (9) in the complex variable A becomes first-order and is reduced to the following dynamical system in three variables $a, q, k = \dot{a}/a$ (the dot denotes differentiation with respect to x):

$$\dot{a} = ka, \tag{11}$$

$$\dot{q} = -c_0(\omega - c_1\mu) + c_0 U_0(q - c_1 k) - 2kq - I_3 a^2, \tag{12}$$

$$\dot{k} = -c_0(c_1\omega + \mu) + c_0 U_0(c_1 q + k) + q^2 - k^2 - R_3 a^2, \tag{13}$$

where $c_0 = 1/(1 + c_1^2)$, $R_3 = c_0(1 - c_1 c_3)$ and $I_3 = c_0(c_3 + c_1)$.

This dynamical system is suited for studying front solutions which do not become zero at some finite x-location. In the following, we describe the trajectories in the phase space (a, q, k), but since they have already been extensively described in previous studies concerning front propagation in infinite domains [15,39–41], we restrict ourselves to the particular features relevant for understanding the NG modes' existence. Although front solutions are correctly described in the phase space (a, q, k), this is not the case for NG modes since they are singular trajectories in this space: k becomes infinite at the origin since $a = 0$ and $\dot{a} \neq 0$. Below, we are led to sometimes use the usual (a, q, k) space and sometimes the slightly different phase space with the variable a, q and $u = \dot{a}$, where NG modes are regular trajectories.

For the analysis of the dynamical system (11)–(13), the frequency ω is considered as a parameter, even though a particular frequency is selected by an NG mode.

2.2.1. The fixed points

This dynamical system possesses three fixed points:

- $A_2 \equiv (a_N, q_N, 0)$ represents the previously introduced traveling wave (with the plus sign dropped); the same symbol A_2 will be used, depending on the context, for the traveling wave of type Eq. (4) and for the associated fixed point $(a_N, q_N, 0)$ in the phase space. In the phase space, A_2 is a saddle and always has a unique stable eigendirection, as shown by van Saarloos and Hohenberg [15], since the condition of positive 'nonlinear group velocity' for the traveling wave $A_2(\omega)$ (Eq. (4)) implies that the stable manifold of the fixed point $A_2(\omega)$ is one-dimensional.

- $A_0^+ \equiv (0, q_0 + \beta, k_0 + \alpha)$ where $q_0 = -c_0 c_1 U_0/2$, $k_0 = c_0 U_0/2$ and

$$\kappa = c_0(\mu + c_1\omega) - \frac{(1 - c_1^2)c_0^2 U_0^2}{4}, \tag{14}$$

$$\sigma = c_0(\omega - c_1\mu) + \frac{c_1 c_0^2 U_0^2}{2}, \tag{15}$$

$$\alpha = \left(\frac{|\kappa + i\sigma| - \kappa}{2}\right)^{1/2}, \tag{16}$$

$$\beta = -\text{sgn}(\sigma)\left(\frac{|\kappa + i\sigma| + \kappa}{2}\right)^{1/2} \tag{17}$$

The stability of A_0^+ is determined from the eigenvalues of the system (11)–(13) linearized around A_0^+. These are the real value $2(k_0 + \alpha)$ with an eigendirection along the a-axis and the complex conjugate eigenvalues $-2(\alpha \pm i\beta)$ with eigendirections spanning the eigenplane $a = 0$. Hence, A_0^+ is a stable spiral in the plane $a = 0$, whereas it is unstable in the a-direction.

- $A_0^- \equiv (0, q_0 - \beta, k_0 - \alpha)$. Similarly, A_0^- possesses the real eigenvalue $2(k_0 - \alpha)$ with an eigendirection along the a-axis and the complex conjugate eigenvalues $2(\alpha \pm i\beta)$ with the eigendirections spanning the plane $a = 0$. A_0^- is an unstable spiral in the plane $a = 0$, and the a-direction is unstable when A_0^- is in the $k > 0$ domain of the (q, k) plane, or stable when A_0^- is in the $k < 0$ domain.

If we had not applied the change of variable Eq. (10), the laminar state $A = 0$ would have been represented by a single fixed point coinciding with the origin of the phase space $A = 0$, $\dot{A} = 0$. When using the phase space (a, q, k), this point $A = 0$, $\dot{A} = 0$ is split into two fixed points A_0^+ and A_0^- which can be given a novel physical interpretation. A physical solution increasing from the laminar state $A = 0$ at minus infinity must correspond to the orbit of the one-dimensional unstable manifold of A_0^+ or A_0^-, which is not embedded in the subspace $a = 0$. When the laminar state $A = 0$ is convectively unstable, A_0^+ and A_0^- may be physically interpreted: the unstable manifold
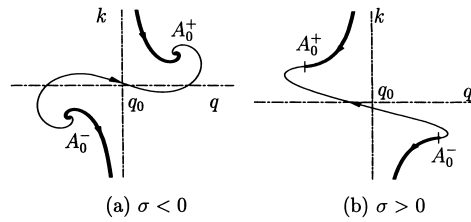
(a) $\sigma < 0$ (b) $\sigma > 0$

Fig. 2. Plane $a = 0$ of the phase space (a, q, k). One bounded heteroclinic orbit (thin curve) between A_0^- and A_0^+ is represented among the infinity which exist and fill the whole plane. The single unbounded trajectories (thick curves) terminating on A_0^+ or starting from A_0^- are called the separatrices (18) and (19) and are asymptotic to $q = q_0$ at $k \to \infty$.

of A_0^+ represents the way to depart from zero when $x \to -\infty$ and the stable manifold of A_0^- represents the way to approach zero asymptotically when $x \to +\infty$. The point A_0^- is associated with the complex quantity $q_0^- - ik_0^-$ which corresponds to the spatial branches propagating information downstream (usually denoted $k^+(\omega)$) [33–35]. Respectively, A_0^+ is associated with the upstream propagation of information usually denoted $k^-(\omega)$. If the laminar state $A = 0$ becomes absolutely unstable, it is no longer possible to associate the different spatial branches with the propagation of information.

2.2.2. The plane $a = 0$

At this stage, it is necessary to describe in detail the plane $a = 0$, which has been shown by Landman [39] to be an invariant subspace of the system (11)–(13). In this plane, an infinite set of bounded heteroclinic orbits linking A_0^- to A_0^+ exist. One of these bounded orbits is displayed as the fine curve in each of Figs. 2(a,b). But an infinity of similar orbits exist between A_0^- and A_0^+, each of them crossing the $q = q_0$-axis at a different value of k. None of the trajectories in the plane $a = 0$ are physical but serve as a footprint of the trajectories slightly off the plane $a = 0$. Any point of the plane $a = 0$ with a finite value of k belongs to one of these trajectories which start from A_0^- and end at A_0^+. We show below that only the unbounded orbits (called the separatrices) in the plane $a = 0$ (thick curves in Fig. 2) describe NG modes since $a = 0$ but $\dot{a} \neq 0$ at $x = 0$, i.e. $k \to \infty$. These separatrices on which k is singular when $x = 0$ are obtained by cancelling the last terms in Eqs. (12) and (13) ($a = 0$) and by solving the Ricatti equation (13)+i Eq. (12) in the variable $k + iq$:

$$q = q_0 + \frac{\beta \sinh(2\alpha x) - \alpha \sin(2\beta x)}{\cosh(2\alpha x) - \cos(2\beta x)}, \tag{18}$$

$$k = k_0 + \frac{\alpha \sinh(2\alpha x) + \beta \sin(2\beta x)}{\cosh(2\alpha x) - \cos(2\beta x)}. \tag{19}$$

The singularity at $x = 0$ is removed by defining the variable u such that

$$u = \dot{a} = ka. \tag{20}$$

Indeed, when Eq. (19) is introduced into Eq. (20) and after integration of Eq. (20), we obtain

$$a = \frac{u_0}{(2|\zeta|)^{1/2}} \exp\left(\frac{c_0 U_0}{2} x\right) (\cosh(2\alpha x) - \cos(2\beta x))^{1/2}, \tag{21}$$

where u_0 is an integration constant and $|\zeta| = \alpha^2 + \beta^2$. It may be seen that $u \to u_0$ when $x \to 0$. The separatrices (18) and (19) associated with Eq. (21) constitute parametric equations for a linear solution of the system (11)–(13) which departs from the plane $a = 0$ with a finite slope $u = \dot{a}$. Eqs. (18) and (19) are simply the projection of this linear solution on the plane $a = 0$.

2.2.3. Front solutions

In the phase space (a, q, k), a front is represented by a heteroclinic trajectory linking A_0^- to A_2 (or exceptionally A_0^+ to A_2). Such fronts exist when the stable manifold of $A_2(\omega)$ intersects the unstable manifold of $A_0^-(\omega)$ which is not embedded in the plane $a = 0$. The stable manifold of $A_2(\omega)$ departs from A_0^- for a continuous set of frequencies and this situation arises for a continuous set of velocities U_0. Therefore, a double family of fronts exist [15], parametrized by the frequency and by the velocity of the front. Among the double family of fronts, a particular front is dynamically selected for fixed μ, c_1, c_3 and will represent the time-asymptotic behavior of the system. For Eq. (1), the selected front has been shown to be the Kolmogorov front [43–45] (terminology borrowed from [44]) and its frequency is the absolute frequency ω_A (Eq. (3)); its velocity is given by Eq. (2). In phase space, the Kolmogorov front corresponds to the unique values of parameters for which $A_0^+ = A_0^-$. Since we have argued that A_0^+ and A_0^- represent different spatial branches of the linear problem, this implies that the front moves such that the instability is at the absolute threshold in the frame moving with the front.

2.2.4. NG modes

In the phase space (a, q, k), an NG mode is represented by a trajectory linking a point of the plane $a = 0$ different from $A_0^\pm$ to A_2. In other words, an NG mode exists when the stable manifold of A_2 intersects the plane $a = 0$ at a point which is not a fixed point. Introduction of this condition in Eqs. (11)–(13) leads necessarily to $q = q_0$ at the intersection point if it exists, since we have required that the prefactors of the diverging k terms need to vanish in Eq. (13). The property $u = \dot{a}$ different from zero at the origin characterizes the existence of an NG mode, which is represented in the (a, q, u) space by a regular trajectory linking a point at finite distance on the axis $(a = 0, q = q_0)$ to A_2. Up to now, we have considered ω as a fixed parameter and, as the stable manifold of $A_2(\omega)$ is one-dimensional, it generically does not cross the axis $(a = 0, q = q_0)$ except possibly for discrete values of ω. Therefore, the existence of a global mode is determined in the (a, q, u) space by searching for an intersection between the axis $(a = 0, q = q_0)$ and the two-dimensional surface formed by the union of each stable manifold of each $A_2(\omega)$ generated by varying ω. The intersection point belongs to a specific stable manifold of a particular $A_2(\omega)$ which defines the selected frequency.

Let us define $\mu_G(U_0, c_1, c_3)$ to be the threshold of emergence of an NG mode, i.e. the smallest value of μ for which the stable manifold of $A_2(\omega)$ intersects the axis $(a = 0, q = q_0)$. This NG instability threshold will be shown first numerically and then analytically to coincide with the absolute threshold μ_A (Eq. (2)), $\mu_A = c_0 U_0^2/4$, the frequency of the NG mode at the threshold being $\omega = \omega_A$. We first describe our observations of the numerically generated phase portraits.

2.3. Phase portraits

We now fix parameters U_0, c_1, c_3 and μ and vary ω in the band of allowed frequencies (ω for which a saturated nonlinear wave exists, represented by the white domain in Fig. 1). Then the fixed point $A_2(\omega)$ describes an arc of a circle in the plane $u = 0$ of the phase space, to which the union of the stable manifolds of $A_2(\omega)$ parametrized by ω is bound. But in the (a, q, u) space, the dynamical system (11)–(13) is transformed into

$$\dot{a} = u, \tag{22}$$

$$a\dot{q} = -2uq - c_0(\omega - U_0 q)a - c_0 c_1(\mu a - U_0 u) - I_3 a^3, \tag{23}$$

$$\dot{u} = aq^2 - c_0(\mu a - U_0 u) + c_0 c_1(\omega - U_0 q)a + R_3 a^3, \tag{24}$$

which is singular when $a \to 0$ although an NG mode is represented by a regular trajectory. Therefore, we are led to numerically compute the trajectories in the four-dimensional phase space $(\text{Re}(A), \text{Im}(A), \text{Re}(\dot{A}), \text{Im}(\dot{A}))$ different
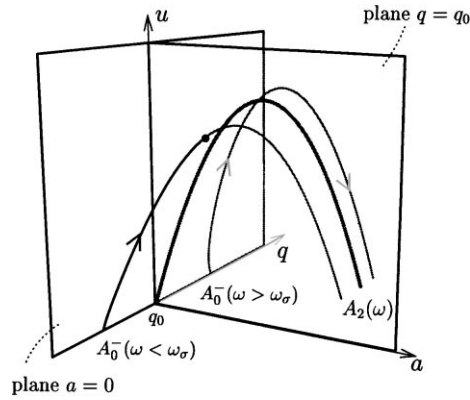
Fig. 3. Stable manifolds of $A_2(\omega)$ in the space (a, q, u) for $\mu = 0.15$ such that $\mu < \mu_A(U_0, c_1)$, with $U_0 = 0.9$, $c_1 = 0.5$, $c_3 = 0.2$. Curves in gray are behind the plane $q = q_0$. The axis $(q = q_0, a = 0)$ may be reached only asymptotically as $x \to -\infty$ for a specific frequency corresponding to the value ω_σ such that $q(A_0^-) = q_0$. The trajectory is then a heteroclinic orbit between $A_0^-(\omega_\sigma)$ and $A_2(\omega_\sigma)$, which does not represent an NG mode as $u = 0$ at the virtual intersection when $x = -\infty$. For any other frequency, the stable manifold of $A_2(\omega)$ emanates from $A_0^-(\omega)$ and either crosses the plane $q = q_0$ at a finite a when $\omega < \omega_\sigma$ (black point at the crossing) or remains behind the plane $q = q_0$ when $\omega > \omega_\sigma$.
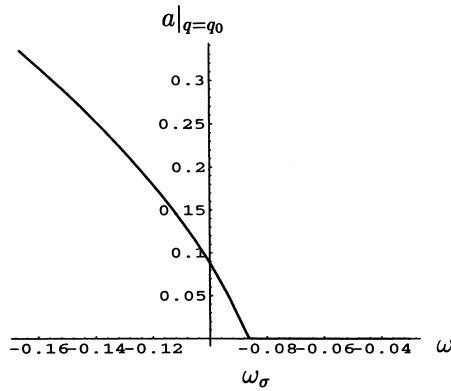

Fig. 4. Amplitude a of the stable manifold of $A_2(\omega)$ at the crossing of the plane $q = q_0$ as a function of ω for the same parameters as Fig. 3. The crossing exists only till $\omega = \omega_\sigma$ for which $a = 0$ only asymptotically at $-\infty$ and therefore $u = 0$.

from the phase space (a, q, u) in which they will be represented. The stable manifolds of $A_2(\omega)$ are computed for each value of ω by a backward numerical integration of Eq. (9) using variable step Runge–Kutta x-integration. For convenience, we will describe the trajectories going backward in x.

When an NG mode exists, it should cross the axis $(a = 0, q = q_0)$ at a finite value of u representing its slope at the origin.

For $\mu < \mu_A$, when ω varies in the white band of Fig. 1 (where a traveling wave of frequency ω exists), no NG mode exists since the stable manifold of $A_2(\omega)$ never crosses the axis $(a = 0, q = q_0)$. Fig. 3 shows three stable manifolds of three different $A_2(\omega)$ for three different values of the frequency. The values of the frequencies are chosen different enough such that the three entire manifolds are clearly distinct. To interpret the observations, let us define ω_σ to be the threshold value such that $\sigma = 0$ (Eq. (15))

$$\omega_\sigma \equiv c_1\mu - \frac{c_1 c_0 U_0^2}{2}. \tag{25}$$
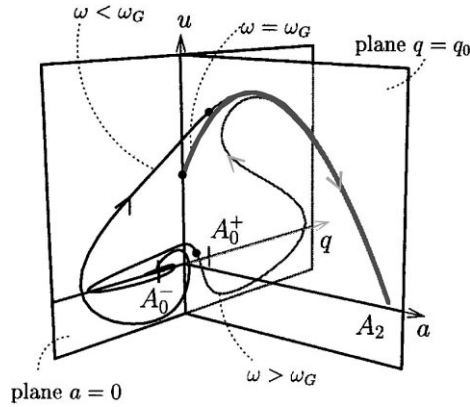
Fig. 5. In the space (a, q, u), three typical stable manifolds of three $A_2(\omega)$ for three different frequencies ω ($\omega < \omega_G$, $\omega = \omega_G$ (thick line), $\omega > \omega_G$), above the NG instability threshold i.e. when $\mu > \mu_A(U_0, c_1)$ ($\mu = 0.6$, $U_0 = 0.9$, $c_1 = 0.5$, $c_3 = 0.2$). The crossing of the axis ($q = q_0$, $a = 0$) occurs for a single value ω_G of the frequency ω. The black points denote the intersection with the plane $q = q_0$ used to construct Fig. 6. Lines in gray are behind the plane $q = q_0$.

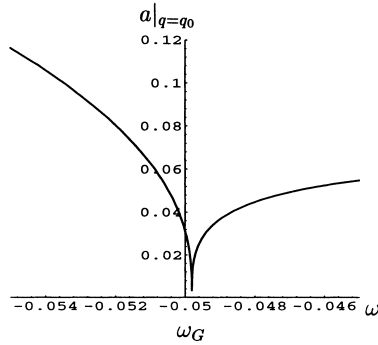Fig. 6. Amplitude $a|_{q=q_0}$ of the stable manifold of $A_2(\omega)$ at the crossing of the plane $q = q_0$ as a function of ω for the same parameters as in Fig. 5. There the cusp in the curve indicates the existence of an NG mode since $a = 0$ and $u \neq 0$.

For $\omega = \omega_\sigma$ (thick curve in Fig. 3), we obtain (only when $\mu < \mu_A$) $q_0^-(\omega_\sigma) = q_0$. Therefore the heteroclinic orbit linking $A_0^-(\omega_\sigma)$ and $A_2(\omega_\sigma)$ does not cross the axis ($a = 0$, $q = q_0$) but asymptotically approaches the point A_0^- on this axis. Therefore, this orbit does not represent an NG mode but a front solution, since the crossing occurs at $u = 0$ when $x = -\infty$. When $\omega < \omega_\sigma$, the stable manifold of $A_2(\omega_\sigma^-)$ crosses the plane $q = q_0$, since $A_2(\omega)$ and $A_0^-(\omega)$ are on each side of the plane $q = q_0$ and the crossing amplitude is not zero. When $\omega > \omega_\sigma$, the stable manifold of $A_2(\omega)$ remains in the half space $q < q_0$ and does not cross the plane $q = q_0$. The fact that no NG mode is obtained for $\mu < \mu_A$ is determined by plotting in Fig. 4 the amplitude a of the stable manifold of $A_2(\omega)$ when it crosses the plane $q = q_0$, as a function of the frequency. For $\omega < \omega_\sigma$, a non-zero value of a is found at the intersection. No cusp is obtained at $\omega = \omega_\sigma$ and for $\omega > \omega_\sigma$, $a|_{q=q_0}$ does not exist.

For $\mu > \mu_A$, the two-dimensional set of stable manifolds of $A_2(\omega)$ intersects the axis ($a = 0$, $q = q_0$) for a particular value of ω determining the selected frequency ω_G of an NG mode. Fig. 5 presents the stable manifolds of three different $A_2(\omega)$ for three values of the frequency ($\omega < \omega_G$, $\omega = \omega_G$ and $\omega > \omega_G$). Since we have chosen three frequencies close to each other in order to show the differences in the three trajectories, the three distinct fixed points $A_2(\omega)$ appear so close to each other that they are indistinguishable and are represented by a single symbol $A_2(\omega)$ in Fig. 5. For $\omega > \omega_G$, the stable manifold of $A_2(\omega)$ avoids the axis ($a = 0$, $q = q_0$) and makes a turnabout
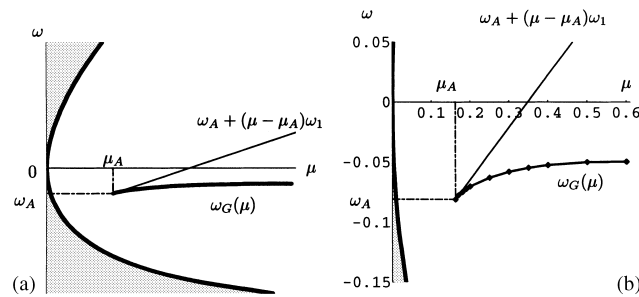
Fig. 7. Selected frequency of the NG modes as a function of μ obtained numerically by integrating the dynamical system (11)–(13), by the method explained in Fig. 5 (thick solid curve) and Fig. 6. Region shown is an enlargement of the zone close to 0 of Fig. 1 (see Fig. 1 caption for explanation of the gray and white regions). NG modes are found to exist only for $\mu > \mu_A$ and their frequency equals $\omega_G(\mu)$, with $\omega_G(\mu_A) = \omega_A$. Parameters are $c_1 = 0.5, c_3 = 0.2, U_0 = 0.9$ (same as Figs. 5 and 6). We predict that $\omega_G(\mu_A) = \omega_A$ and the slope of $\omega_G(\mu)$ (thin line) by a singular perturbation analysis around the threshold. (b) Results discussed in Section 4, found by a full numerical simulation of the partial differential Eq. (1) have been added. The diamonds are frequency values found by these temporal simulations after transient behaviour has died out.

in the half space $q > q_0$ (gray curve in Fig. 5) before crossing the plane $q = q_0$ at a finite value of a. It then spirals into A_0^- in the half space $q < q_0$. For $\omega < \omega_G$, it crosses the plane $q = q_0$ at a finite value of a and immediately spirals into A_0^-. When ω equals exactly ω_G, the stable manifold of $A_2(\omega_G)$ crosses the plane $q = q_0$ exactly on the axis $(a = 0, q = q_0)$ at a finite value of u. It is quite remarkable that this singular trajectory insures a smooth transition between the two configurations described above.

To find the precise value ω_G for which the intersection with the axis $(a = 0, q = q_0)$ occurs, and to obtain a criterion for the existence of an NG mode, we have plotted systematically as in Fig. 6 the amplitude a of the stable manifold of $A_2(\omega)$ when it crosses the plane $q = q_0$, as a function of the frequency ω. Around a single value $\omega_G(\mu, U_0, c_1, c_3)$, this amplitude can approach zero arbitrarily closely depending only on the resolution we use to span the ω axis, as indicated by the cusp in Fig. 6. We have verified that at the value ω_G given by the criterion sketched in Fig. 6, the slope u of the solution at the origin is non-zero.

The analysis of the phase portraits for all $\mu > \mu_A$ and the frequency selection criterion sketched in Fig. 6 locate numerically for each set of parameters U_0, c_1, c_3 the curve ω_G as a function of μ represented in Fig. 7. This selected frequency $\omega_G(\mu)$ plotted as the thick solid curve in Fig. 7 starts from the absolute frequency ω_A at the absolute threshold μ_A, showing that the NG threshold coincides with the threshold of absolute instability μ_A; this observation will be proven by the perturbation analysis presented in the next section which also predicts the leading order and the next order of the frequency, i.e. the slope ω_1 at μ_A (thin solid line $\omega = \omega_A + (\mu - \mu_A)\omega_1$).

3. Proof of the existence of a global mode for $\mu > \mu_A$ and scaling laws

We propose here to turn the numerical and graphical observations for the occurrence of an NG mode into a proof of the existence of a global mode for $\mu > \mu_A$, by performing a singular perturbation analysis near the threshold of global instability. This threshold is the absolute threshold μ_A and is also the control parameter for which a Kolmogorov front of velocity $-U_0$ (i.e. able to withstand the advection) would be selected in an infinite domain. For the front selection problem, the boundary condition at the origin is relaxed and, since the medium is unstable, a front develops between the unstable amplitude state $A = 0$ (on the left) and the stable state A_2 (on the right). The front propagates to the left at a constant velocity given by the linear marginal stability criterion [46]. This criterion is equivalent to the determination of the absolute instability of the leading edge of the front $A = 0$ in the reference frame where the front is stationary. Therefore, the relation between μ_A and a fixed advection velocity in a

semi-infinite domain is the same as the link between the control parameter μ and the Kolmogorov front velocity in an infinite domain. For a fixed advection velocity (to the right) and for $\mu > \mu_A$, the Kolmogorov front propagates to the left until it stops near the boundary $x = 0$ to match the condition at the origin. We will therefore perform the perturbation analysis around the Kolmogorov front solution at $\mu = \mu_A$, which represents the marginal NG mode at threshold, and show for $\mu < \mu_A$ that no NG mode exists, and compute for $\mu > \mu_A$ the NG solution. The analysis predicts for fixed parameters, U_0, c_1, c_3 the leading and first order of the frequency $\omega_G(\mu)$ (see Fig. 7) at the threshold and the growth length of the NG modes, defined as the distance at which the amplitude reaches 50% of its maximum value, as a function of the distance from the NG instability threshold. However, since the first order of the frequency will be given by the numerical estimate of an analytical matching condition (Eq. (29) below), a case-by-case calculation must be carried out for each set of parameters to prove the existence of an NG mode for $\mu > \mu_A$.

In the phase space (a, q, u), we are looking for the stable manifold of $A_2(\omega)$ which at $\omega, \mu, c_1, c_3, U_0$ fixed may be parametrized by a. The reason for considering this phase space and not (a, q, k) as already discussed is that we wish to obtain regular trajectories near $a = 0$ for the global modes. The trajectory $q_f(a), u_f(a)$ at $\mu = \mu_A$ and $\omega = \omega_A$ represents the Kolmogorov front solution, i.e. the heteroclinic orbit linking $A_0^- = A_0 = (0, q_0, 0)$ to $A_2(\omega_A)$. It is similar to the orbit corresponding to ω_σ presented in Fig. 3 in Section 2. The parametric representation $q_f(a)$ and $u_f(a)$ are expressed as a series in a with terms $\rho_j(a_N - a)^j$ and $v_j(a_N - a)^j$, where a_N denotes the amplitude of $A_2(\omega_A)$ to which the Kolmogorov front is asymptotic. For simplicity, unless otherwise stated, a_N and q_N denotes in this section $a_N(\omega_A)$ and $q_N(\omega_A)$, evaluated at $\mu = \mu_A$. When setting the bifurcation parameter value to $\mu = \mu_A + \epsilon$, the stable manifold of $A_2(\omega)$ is considered as a perturbation of the solution $q_f(a), u_f(a)$ and the perturbation is also taken in the form of series expansions with general terms $\epsilon \eta_j(\omega)(a_N - a)^j$ and $\epsilon \lambda_j(\omega)(a_N - a)^j$, respectively. This perturbed solution satisfies the boundary conditions at infinity, i.e. it asymptotically approaches $A_2(\omega)$ along its unique stable eigendirection. It constitutes the outer solution of the problem which should be matched with the proper inner solution valid around $a = 0$.

In the singular limit $\epsilon \to 0$, an inner region of size $\theta(\epsilon)$, $\theta(\epsilon)$ being a function vanishing with ϵ to be determined by the matching, is introduced in the neighborhood of the origin in order to take into account the boundary condition $a(0) = 0$. An inner solution is represented as the linear solutions (18), (19) and (21) of system (11)–(13) in the vicinity of $a = 0$.

Application of the method of matched asymptotic expansions [47] between the inner and the outer solution should give rise to an NG mode determined by the intersection of the perturbed solution and of the axis $(a = 0, q = q_0)$. This mode corresponds to a single frequency of the form $\omega_A + \epsilon \omega_1$. The matching leads to the determination of the slope $u = v_0$ at the origin $(x = 0)$, the growth length of the NG mode and the departure $\epsilon \omega_1$ of the NG mode frequency from ω_A.

We proceed to a detailed analysis of the outer and inner solutions in Appendix A.

3.1. Matching

In order to determine the unknown integration constant v_0 which appears in the inner solution (its slope at the origin) and the departure $\epsilon \omega_1$ of the frequency of the NG mode from ω_A, we match the outer quantity $u_o(a)/a + iq_o(a)$ given by Eqs. (A.10) and (A.11) and the inner expression $k_i + iq_i$ given by Eq. (A.15). At order zero, we obtain three solvability conditions which read

$$\sum_{j=0}^{+\infty} v_j a_N^j = 0, \qquad \sum_{j=0}^{+\infty} \rho_j a_N^j = q_0, \qquad -\sum_{j=0}^{+\infty} j v_j a_N^{j-1} = k_0. \tag{26}$$

These equations simply mean that the Kolmogorov front departs from $a = 0$ with asymptotic wavenumber q_0 and slope k_0 at $x \to -\infty$, i.e. varies as $\exp[(k_0 + iq_0)x]$. They are satisfied only when $\epsilon \geq 0$. Therefore, no NG mode exists for $\epsilon < 0$. The matching at the next order ($\mathcal{O}(\epsilon^{1/2})$) imposes the size of the inner layer

$$\theta(\epsilon) = \epsilon \exp\left(-\frac{c_0 U_0 \pi}{2\beta_1 \sqrt{\epsilon}}\right), \tag{27}$$

and the condition characterizing the matching of the departure of the NG mode (wavenumber and slope) from the Kolmogorov front, at the border between the inner and outer layers:

$$\alpha_1 + i\beta_1 = \frac{|\zeta_1|^{1/2}}{v_0} \sum_{j=0}^{+\infty} \lambda_j a_N^j - i\frac{v_0}{|\zeta_1|^{1/2}} \sinh^2\left(\frac{\alpha_1 \pi}{\beta_1}\right) \sum_{j=1}^{+\infty} j\rho_j a_N^{j-1}, \tag{28}$$

with $|\zeta_1| = (c_0(1+\omega_1^2))^{1/2}$, $\alpha_1 = ((|\zeta_1| - \kappa_1)/2)^{1/2}$, $\beta_1 = ((|\zeta_1| + \kappa_1)/2)^{1/2}$, and $\kappa_1 = c_0(1+c_1\omega_1)$ (see Appendix A). The coefficients λ_j are linear in ω_1: $\lambda_j = \lambda_j^0 + \omega_1 \lambda_j^1$. Modulus and phase identification of Eq. (28) determine v_0 and ω_1. An equation involving only ω_1 is found by multiplying real and imaginary parts of the l.h.s. and r.h.s. of Eq. (28) and reads

$$\alpha_1 \beta_1 = -\sinh^2\left(\frac{\alpha_1 \pi}{\beta_1}\right) \sum_{j=1}^{+\infty} j\rho_j a_N^{j-1} \sum_{j=1}^{+\infty} (\lambda_j^0 + \omega_1 \lambda_j^1) a_N^j. \tag{29}$$

The frequency shift ω_1 is numerically evaluated as the solution of Eq. (29), giving the selected frequency $\omega_G \simeq \omega_A + \epsilon\omega_1$. This second order prediction is plotted as the fine solid line on Fig. 7, for which we obtain $\omega_1 = 0.433$, and that indeed asymptotically approaches the curve of ω_G as a function of μ found by integrating the ordinary differential equations (11)–(13). We are now able to find scaling laws for the growth length of NG modes and for their slope $|da/dx(0)|$ at the origin of the domain as a function of ϵ, the distance from the NG threshold $\mu - \mu_A$.

The slope v_0 of NG modes is determined by Eq. (28) and rescaled by the size of the inner region:

$$\log\left|\frac{da}{dx}(0)\right| \simeq -\frac{c_0 U_0 \pi}{2\beta_1 \sqrt{\epsilon}} + \log\epsilon + \log v_0. \tag{30}$$

The dominant contribution as $\epsilon \to 0$ is the $\epsilon^{-1/2}$ term and this result is analytic although the coefficient β_1 depending on ω_1 may only be numerically computed from Eq. (29).

The growth length of the global mode is defined as the distance Δx such that $a(\Delta x) = 0.5 a_N$. It is calculated by adding the x-thickness of the inner region and the size of the outer solution between the boundary of the inner layer and the point at which the amplitude reaches the value $0.5 a_N$. Since at the upstream edge in the outer layer, the spatial growth of the NG mode is exponential, its outer contribution to the growth length is of order $\log(1/\epsilon)$. Therefore, the dominant contribution comes from the inner layer:

$$\Delta x \simeq \frac{\pi}{\beta_1 \sqrt{\epsilon}}. \tag{31}$$

The $\epsilon^{-1/2}$ dependence emerges naturally from the singular perturbation analysis and may be physically interpreted as the spatial beating of the two linear waves at frequency $\omega_A + \epsilon\omega_1$ and wavenumbers differing by a $\sqrt{\epsilon}$ quantity. In the real case ($c_1 = c_3 = 0$), $\beta_1 = 1$ and the above scaling laws (30) and (31) have been validated in a previous study [3,4] by numerical integration in x of the trajectory in the phase space given by the ordinary differential Eqs. (11)–(13). Before proceeding to the comparison of the scaling laws with results from full numerical simulation of the partial differential equation (1) for non-zero value of the parameters (c_1, c_3), we wish to point out that some recent results on front propagation might bear on the scaling laws investigated here. Brunet and Derrida [48]

have studied the effect of a small cutoff h on the front velocity selection. They have shown that the front velocity converges slowly to its asymptotic value when $t \to +\infty$, and that the shift in velocity from its asymptotic value varies logarithmically with the cutoff h. In the present study, the boundary condition $A(x = 0) = 0$ represents the ideal case of an open flow without noise at the inlet. It may be replaced by another boundary condition without loss of generality. For example with the condition $|A|(x = 0) = h$, the existence of an NG mode will be given similarly by the intersection in the phase space of the stable manifold of the asymptotic state when $x \to +\infty$ (a traveling wave) with the set representing the boundary condition (the plane $|A| = h$). It can be shown that an NG mode will exist for all h and that the growth length of the NG mode will depend logarithmically on h, since the $1/\sqrt{\epsilon}$ scaling comes from the inner layer, which is not necessary when $|A|(x = 0) = h$. The later logarithmic scaling, valid for the length of the NG mode withstanding a fixed advection velocity, is very similar to the scaling of the shift in the front velocity found by Brunet and Derrida. Ebert and van Saarloos [49] have shown, that the relaxation of fronts towards their asymptotic shape and velocity is algebraic in time, when $t \to +\infty$. We have not studied here the speed of convergence from a given initial state towards the NG mode, but the result should be as in reference [49], since Ebert and van Saarloos have used similar arguments as in the present study in order to compute the departure of the front shape from its asymptotic shape.

4. Simulations

Up to this point in the present paper, only existence of time-periodic solutions (NG modes) of Eq. (1) has been investigated numerically and theoretically. Although numerical integrations of the dynamical system (11)–(13) confirm the validity of the matched asymptotic expansion analysis and demonstrate the essential result that an NG mode exists only when the basic state is linearly absolutely unstable, they tell us nothing about the stability of the NG modes, their basin of attraction or about the existence of other (not time-periodic) solutions. We will therefore compare our results with numerical simulations of the partial differential equation (1). Simulations are performed with $A(0) = 0$ and the boundary condition at the outlet ensuring that the solution is asymptotic to any traveling wave (i.e. we impose equality between the ratio of the amplitudes $A(x+dx, t+dt)/A(x, t) = A(x, t)/(A(x-dx, t-dt))$ [50]). The implicit Crank–Nicholson scheme [51] is used to perform the simulations. As explained in [52], the time and space steps must be chosen sufficiently small to ensure that the nature of the instability is not altered by the numerical scheme. The initial state of the system is $A(x) \equiv 0$ for all x and a very small perturbation is added. The simulation is run until all transients die out. Due to the strong regulating effect of the advection, the asymptotic state of the system is found to be insensitive to the choice if the initial condition.

In order to test the validity of our analysis, we first compare the results given by numerical simulations of the partial differential equation (1) with those obtained in Section 2 from the phase portrait analysis on one hand, and with those obtained by the matching in Section 3 on the other hand. This will confirm that the NG mode is indeed the attractor of the system when it exists. When the NG mode does not exist, the solution asymptotically returns to zero for each x, no matter what the initial condition is. When the NG mode exists but is unstable, the asymptotic solution of the evolution equation (1) is more complex and usually not time-periodic. We determine next the region of parameter space in which a stable NG mode is found by simulations of Eq. (1) and show that the border of this region is given by the change of nature of the secondary instability (from convective to absolute) of the traveling wave to which the NG mode is asymptotic at infinity.

4.1. Validation of the scaling laws

Fig. 7(b) shows the frequency of the NG modes obtained by the above-mentioned three methods. For $U_0 = 0.9$, $c_1 = 0.5$, $c_3 = 0.2$, we vary μ from below the threshold $\mu_A = 0.162$ to $\mu = 0.6$. For $\mu < \mu_A$, the solution
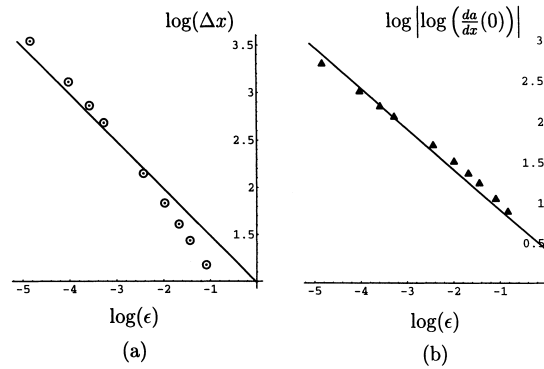
Fig. 8. Growth length (a) and slope at the origin (b) of the NG modes for different values of the criticality ϵ and $c_1 = 0.5$, $c_3 = 0.2$, $U_0 = 0.9$. The straight lines represent the scaling laws obtained from the analytical matching and the dots result from a temporal simulation of Eq. (1). Note that the theoretical law is derived without any adjustable parameter.

relaxes back to zero for all the initial conditions tested. For each $\mu > \mu_A$, we report the frequency $\omega_G(\mu)$ obtained by numerical integration of the dynamical system (11)–(13) (thick curve), for which the stable manifold of $A_2(\omega)$ crosses the axis ($a = 0$, $q = q_0$ but $u \neq 0$) of phase space, as found by the criterion presented in Section 2, Fig. 6. For the same values of μ, we perform a temporal simulation of the partial differential equation (1), following the protocol explained above. The modulus of the amplitude grows and evolves to an NG mode as for the real Ginzburg–Landau model [3,4]. When the amplitude modulus has become steady, we measure the frequency of the NG mode. It is quite remarkable that these numerical measurements, plotted as diamonds in Fig. 7(b), lie exactly on the curve corresponding to the frequencies obtained by the phase portrait analysis. Finally, the leading order of $\omega_G(\mu)$, $\omega_G \sim \omega_A + \omega_1 \epsilon$, computed by Eq. (29) as given by our singular perturbation analysis (straight fine line in Fig. 7(b)) is in excellent agreement with the results found numerically since it is tangent to the numerical curve at $\mu = \mu_A$.

In the simulations of the partial differential equation (1), when the long time regime is reached, we also measure the growth length of the NG mode and its slope at the origin as a function of the departure ϵ from the NG instability threshold. The numerical values (dots in Figs. 8(a,b)) are found to be in good agreement with the theoretical scalings determined without any adjustable parameter $\Delta x \sim (\pi/\beta_1)\epsilon^{-1/2}$ and $\log|\mathrm{d}a/\mathrm{d}x(0)| \sim -(c_0 U_0 \pi/2\beta_1)\epsilon^{-1/2}$ (Eqs. (31) and (30)), and represented by the straight lines to which they should be asymptotic when $\log(\epsilon) \to -\infty$. This three-fold test not only confirms the validity of the singular perturbation analysis, but it also indicates that the NG mode is the attractor of the dynamics and, in doing so, it validates the frequency selection criterion of Section 2 far from threshold. For fixed parameters U_0, c_1, c_3, μ, the phase portrait analysis is far easier to handle, faster and more precise than a numerical simulation of the partial differential equation (1), and predicts exactly the NG mode frequency which will be selected in a temporal simulation. Let us emphasize again that this phase portrait analysis not only determines the spatial profile of the NG mode, but also constitutes a nonlinear frequency selection criterion.

4.2. Comparison with results from the Rayleigh–Bénard and Taylor–Couette problems

It is not obvious that the scaling laws derived analytically in Section 3.1 and verified in Section 4.1 by integration of the dynamical system (11)–(13) and by temporal simulation of the partial differential equation (1) apply to the description of real flows. To test the relevance of the present model to describe experimental situations, we have interpreted the pattern selection occurring in two particular open flows.

Büchel et al. [11] have numerically computed the propagating vortex structures in the rotating Taylor–Couette system with an externally imposed axial throughflow. When studying the flow between two concentric cylinders, the outer one at rest and the inner one rotating at a constant velocity, the bifurcation parameter called the Taylor number measures the rotation rate of the inner cylinder. Above a critical Taylor number, the system exhibits toroidal vorticity rolls associated with the breaking of z-invariance (the direction of the axis of the cylinders). Büchel et al. [11] have shown numerically that the addition of a throughflow possesses a strong regulating effect: the critical Taylor number above which vortex rolls can be observed increases with the Reynolds number, which measures the intensity of the throughflow. Above threshold, the vortices are axisymmetric and propagate downstream, their structure being uniquely selected, i.e. independent of parameter history, initial conditions or system size. The deviation of the axial velocity component from the basic state as a function of the streamwise coordinate exhibits a stationary envelope. Its amplitude grows from $A = 0$ at the origin, saturates and rapidly decreases to match the outlet boundary condition $A(L_b) = 0$. Except near the boundaries, the amplitude is a saturated propagating wave representing the propagating vortices. The numerical simulations of two-dimensional Navier–Stokes equations for the Taylor–Couette problem with throughflow by Büchel et al. have measured the growth length from the inlet, i.e. the length necessary to reach half the maximum amplitude. They show that the dynamics of the system may be interpreted by simulations of the Ginzburg–Landau equation (1) associated with boundary conditions $A(0) = 0$ and $A(L_b) = 0$. Therefore, they have derived the complex Ginzburg–Landau equation by a weakly nonlinear analysis of the Taylor vortices in axial throughflow and they have computed the coefficients U_0, μ, c_1, c_3 as functions of the Reynolds and Taylor numbers, using fit formulas valid for small Reynolds numbers [53]. Temporal numerical simulations of the Ginzburg–Landau equation show that above threshold, the solution represents precisely the amplitude of Taylor–Couette vortices in the presence of a throughflow, obtained by temporal numerical simulations of Navier–Sokes equations. The numerically obtained growth length of solutions of the Ginzburg–Landau equation is in good agreement with the growth length obtained by simulations of Navier–Stokes equations for the Taylor–Couette problem with throughflow. In particular, they observe a divergence of the growth length when approaching the instability threshold, which they identify as the border between convective and absolute instability of the basic Taylor–Couette flow with an added annular throughflow. We will show that the power law (31) compares satisfactorily with their numerical measurements of the growth length of NG modes obtained for the Taylor–Couette problem with throughflow by Büchel et al. [11]. Before the comparison, let us describe measurements for another open flow also leading to a good agreement with power law (31).

Müller et al. [12,13] have performed a similar numerical simulation for the Rayleigh–Bénard problem with an added Poiseuille flow. When a critical temperature gradient, measured by the Rayleigh number, is exceeded, the Rayleigh–Bénard system exhibits convection rolls which break the translation symmetry. The birth of these rolls has been described by Fineberg and Steinberg [25], as a convective vortex front propagating into the unstable basic conductive state. Using numerical simulations of the two-dimensional Navier–Stokes equations, Müller et al. [12,13] show that addition of a throughflow to a fluid layer heated from below also possesses a strong regulating effect: the critical Rayleigh number above which convection rolls are obtained increases with the Reynolds number. Above threshold, the vertical velocity field exhibits a stationary envelope as for the Taylor–Couette problem, which may be described as the solution of a complex Ginzburg–Landau equation with associated boundary conditions $A(0) = 0$ and $A(L_b) = 0$, since the basic flow is enforced at the inlet and at the outlet of the domain. They compute the coefficients of Eq. (1) as functions of the Rayleigh and the Reynolds numbers, and show that the growth length obtained by temporal simulation of Eq. (1) is in agreement with the results obtained from temporal simulations of Navier–Stokes equations. As for the Taylor–Couette problem, we will show that the power law (31) satisfactorily compares with numerical measurements of the growth length of NG modes obtained for the Rayleigh–Bénard flow with an added Poiseuille flow by Müller et al. [12,13],
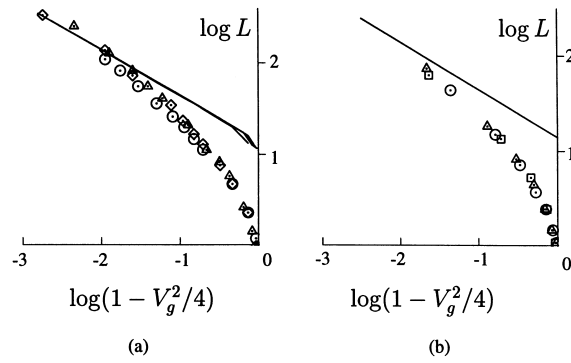
Fig. 9. (a) The scaled growth length of NG modes predicted by Eq. (32) (solid lines) are superposed on the results of [11]. For Taylor–Couette problem with throughflow, the three sets of open symbols represent values computed [11] for three different Taylor numbers. (b) The same quantities for the Rayleigh–Bénard problem with throughflow. Symbols represent values computed [12,13] for three different Rayleigh numbers. The solid line is our theoretical $\epsilon^{-1/2}$ law with $\beta_1 = 1$.

In both the studies by Büchel et al. and those by Müller et al., a graph of the growth length L is presented as a function of the scaled advection velocity V_G. In order to obtain a quantitative comparison, we have rewritten power law (31) in the form

$$L \simeq \frac{\pi}{\beta_1} \left(1 - \frac{V_g^2}{4}\right)^{-1/2},$$ (32)

using the transformations $L \equiv \sqrt{\mu}\Delta x$ and $V_g \equiv U_0\sqrt{c_0/\mu}$ coming from the nondimensionalization of the equation. The expression $1 - V_g^2/4$ is the rescaled departure from criticality. For the Taylor–Couette problem, we have used in Eq. (32) the same values of the Reynolds Re and Taylor T numbers as those plotted in Fig. 1 by [11] to generate for each combination (Re, T), the set of Ginzburg–Landau coefficients U_0, c_1, c_3 given in [11]. This allows us to compute the precise value of β_1 from Eq. (28). Since the values of the coefficients c_1 and c_3 used by Büchel et al. and Müller et al. are small ($c_1 \sim \mathcal{O}(10^{-2})$ and $c_3 \sim \mathcal{O}(10^{-3})$), β_1, may be well approximated by one. For this reason, a real model of amplitude equation for which $\beta_1 = 1$ would have been sufficient to obtain the same scalings.

Our theoretical results are superposed on those obtained by Büchel et al. [11] in the log–log plot of Fig. 9(a). As shown in Fig. 9(a), the growth length L of the Taylor–Couette vortices versus the scaled advection velocity V_g is in excellent agreement with our scaling law (31), which is supposed to be valid for $\log(1 - V_g^2/4) \to -\infty$. Since there is no adjustable parameter in the derivation of Eq. (32), this confirms the validity of our analysis to describe the dynamics of Taylor–Couette system with throughflow.

The same quantitative agreement is observed when we compare our theoretical analysis with the numerical results of Müller et al. [12,13] for the Rayleigh–Bénard problem with throughflow (Fig. 9(b)). Reynolds and Rayleigh numbers identical to those used by Müller et al. are chosen to generate for each (Re, Ra) pair the set of Ginzburg–Landau coefficients U_0, c_1, c_3 given in [13]. The precise value of β_1 is computed from Eq. (28). Since the numerical simulations by Müller et al. are done in a box of small size L_b, a linear stability analysis shows that there exists a shift on the global instability threshold proportional to $1/L_b^2$ [54–56]. As a result, the theoretical threshold valid for an infinite domain cannot be approached more closely than a quantity varying as $1/L_b^2$. This remark is also valid for the numerical results of the Taylor–Couette problem by Büchel et al. [11]. The difference of size L_b between the two problems explains why the closest point to the threshold obtained in the simulations of the Rayleigh–Bénard problem by Müller et al. is further from the closest point to the threshold obtained in the simulations of the Taylor–Couette problem by Büchel et al. However, there is again no free parameter and the slope

as well as the position of the theoretical power law (32) is in agreement with the numerical measurements by Müller et al.

4.3. Stability of the NG modes

NG modes exist beyond the threshold of the primary bifurcation which coincides here with the threshold of local absolute instability of the flow. They give rise to a saturated state which presents a periodic structure in the direction of the flow. It is natural to consider the stability of the NG modes, i.e. the secondary bifurcation of the flow. As for the primary bifurcation which is determined by the global instability of the basic state $A = 0$, the secondary bifurcation may be determined by the global instability of the NG mode. Since an NG mode consists of a growing front and a traveling wave $A_2(\omega_G(\mu))$ to which it is asymptotic as $x \to \infty$, we will denote these two parts as the 'core' and the 'wing' of the NG mode. This terminology is usually adopted for Nozaki–Bekki holes [30,57] and for dark solitons [58].

As we will see, the relevant concept for determining the global instability of an NG mode (the secondary global bifurcation of the flow) here is the absolute or convective nature of the local instability of its wing [59,60]. We will first recall the temporal stability properties of the traveling waves (4) which are solutions of the Ginzburg–Landau equation, and we will determine the nature (absolute or convective) of the unstable saturated waves. We will next apply the result to the wing $A_2(\omega_G)$ of the selected NG mode when the bifurcation parameter varies, and then to the particular traveling wave $A_2(\omega_A)$ at $\mu = \mu_A$ to determine whether the wing of the NG mode at the primary bifurcation threshold is absolutely or convectively unstable (or stable). We will then show that two different scenarios for the route to disorder may occur: a direct transition when $A_2(\omega_A)$ at $\mu = \mu_A$ is absolutely unstable, or else a sequence of bifurcations when it is stable or convectively unstable. To test these two scenarios for the secondary bifurcation of the flow, we will numerically simulate the partial differential equation (1). Initially, small perturbations will be added to the basic state $A(x) = 0, \forall x$. If the system saturates and reaches at long times an NG mode, then the NG mode is stable and increasing the bifurcation parameter should determine numerically the second bifurcation and confirm that they are obtained sequentially. If the system does not converge to an NG mode but to a more complex solution, then the NG mode which exists for the same parameters is unstable.

4.3.1. Temporal stability of traveling waves

The linear temporal stability of the traveling waves (4) has been examined by Matkowsky and Volpert [36] for long waves and finite wavelength perturbations. Their results may be recalled using the wavenumber q_N as a parameter for the family of Stokes solutions of type Eq. (4) that exist at given (μ, c_1, c_3). Before proceeding with the stability limits, let us rescale

$$q^* = q\mu^{-1/2}, \qquad a^* = a\mu^{-1/2}, \qquad U_0^* = U_0\mu^{-1/2}, \tag{33}$$

which allows us to set μ to unity. This rescaling has not been done earlier in order to facilitate the comparison with experiment and to distinguish the effect of the advection velocity from the effect of the bifurcation parameter in the scaling laws for the growth length and the slope of the NG modes, but its use will clarify the remainder of our study. This rescaling is equivalent to increasing the bifurcation parameter at fixed advection velocity or, alternatively, to decreasing the advection velocity at fixed μ, each operation representing a reduction of the rescaled advection velocity U_0^*.

When only temporal stability is considered, the problem is further simplified since a Galilean transformation allows us to set U_0^* to zero. This will not be true when spatiotemporal instability or fronts are considered. The traveling waves of type Eq. (4) are linearly unstable in the Benjamin–Feir unstable domain $1 - c_1 c_3 < 0$. In the domain $1 - c_1 c_3 > 0$, the traveling waves of type Eq. (4) are stable if their wavenumber satisfies $q_N^{*2} < q_E^{*2}$, (denoted
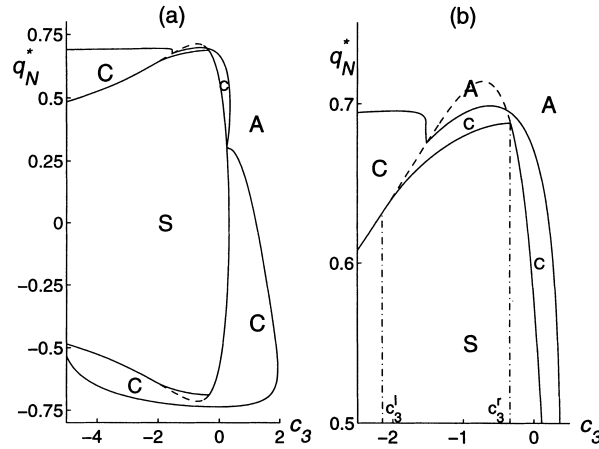
Fig. 10. Regions of stability (S), convective (C) and absolute (A) instability of traveling waves in the plane (q_N^*, c_3) for $c_1 = 3$. The traveling wave with rescaled wavenumber q_N^* is linearly stable within the S region. The dashed line extends the S region when only longwave perturbations are taken into account. (a) The convective instability boundary is computed for $U_0^* = 2$. (b) Enlargement of (a) in the region where the waves are stable to long wave perturbations but unstable to finite wavelength perturbations for $c_3^l \leq c_3 \leq c_3^r$ (upper right corner of (a)).

below as the Eckhaus stable band). Matkowsky and Volpert [36] have found that the neutral Eckhaus wavenumber $q_E^*(c_1, c_3)$ is a different function of parameters when the loss of stability is due to long wave perturbations, in which case the neutral Eckhaus wavenumber is given by

$$q_E^{*2} = \frac{1 - c_1 c_3}{3 + 2c_3^2 - c_1 c_3}, \tag{34}$$

or when it is due to finite wavelength perturbations, in which case an explicit expression of the neutral Eckhaus wavenumber may be derived from the analysis by Matkowsky and Volpert and is given by Eq. (B.2) in Appendix B. The boundaries of the region in the (c_1, c_3) plane to which it pertains are also derived from Matkowsky and Volpert and are given by Eq. (B.1) in Appendix B.

In Fig. 10, we have let c_3 vary and we have plotted the stability boundary of traveling waves $A_2(\omega)$ represented by the rescaled wavenumber q_N^* as a function of c_3, for the parameter $c_1 = 3$ (and $\mu = 1$ due to the rescaling Eq. (33)). The stability region (S) is bounded by the neutral Eckhaus wavenumber q_E^*. The instability is due to long wave perturbations in the whole domain (q_E^* given by Eq. (34)) except in a small band $c_3^l < c_3 < c_3^r$ (see enlargement in Fig. 10(b)), where it is due to finite wavelength perturbations. In this band q_E^* is given by Eq. (B.2) and remains below the value given by Eq. (34) represented in dashed line. As a result, within the region bounded by the dashed line and by the solid line limiting the stability region in Fig. 10, the saturated traveling waves are linearly unstable, whereas the classical analysis taking solely into account long wave perturbations, would have led to the conclusion that these waves are in the Eckhaus stable band.

4.3.2. Absolute and convective instability of the traveling waves

Matkowsky and Volpert have only considered temporal instability but since we are considering a problem where Galilean invariance is broken by the inlet condition, we should extend their analysis and consider whether the instability is convective or absolute.

The absolute or convective nature of the traveling wave is determined classically [62] by considering perturbations of the form:

$$a(x, t) = a_N + a_1(x, t), \qquad \theta(x, t) = q_N x - \omega t + \theta_1(x, t) \tag{35}$$
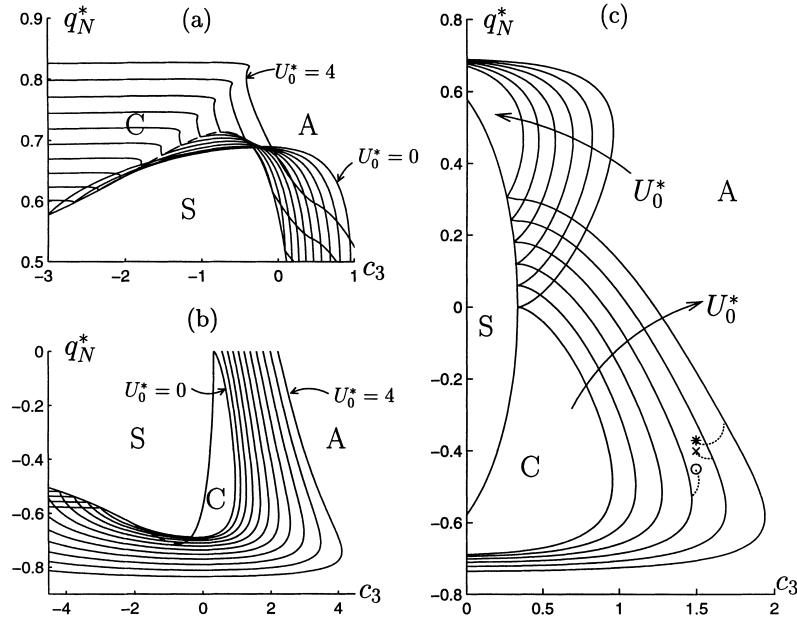
Fig. 11. Same as in Fig. 10 but for different rescaled advection velocities. Each line bounds the region of convective instability of the traveling waves for a fixed velocity $U_0^* \equiv \mu^{-1/2} U_0$. Different scales have been used in each plot (a), (b) and (c) referring to different region of the plane (q_N^*, c_3). In (a) and (b), U_0^* goes from 0 to 4 with a step of 0.4. In (c), U_0^* goes from 0 to 2 with a step of 0.4; the cross and the star refers to the simulations in the convective region for $c_3 = 1.5$, $U_0^* = 2$ (star) and $U_0^* = 1.6$ (cross-referring to simulation in Fig. 12(a)). The circle refers to simulation Fig. 12(b) with $U_0^* = 1.2$; in the latter case, the NG mode is unstable but q_N has still been measured from the oscillation frequency close to the origin.

with $a_1(x, t)$ and $\theta_1(x, t)$ proportional to $\exp(-i\Omega t + iKx)$. The dispersion relation reads:

$$\Omega(K) = -iK^2 + (U_0 + 2q_N c_1)K - ia_N^2 + i((1 + c_3^2)a_N^2 - (c_1^2 K^2 - 2iq_N K - c_3 a_N^2)^2)^{1/2}, \tag{36}$$

where a_N, q_N are given by Eqs. (5) and (6) and the perturbation frequency Ω, and wavenumber K are complex. Only the phase branch is considered, since it is the only one to become unstable. Using the form (35) for the perturbations, one obtains a linear equation with constant coefficients and therefore avoids Floquet analysis [63] which generically determines the secondary bifurcation of a periodic state [61].

Using Matlab and the built-in rootfinder of systems of equations, we seek the neutral saddle points $\Omega_0 = \Omega(K_0)$, $d\Omega/dK(K_0) = 0$ such that $\Im(\Omega_0(K_0)) = 0$ by the 'pinching' process (see [33,34]), which defines the boundary between absolute and convective instability for the traveling wave $A_2(\omega)$. This boundary is represented in Fig. 10 by the reduced wavenumber $q_N^* \equiv q_N \mu^{-1/2}$ as a function of c_3, for the parameter $c_1 = 3$ and advection velocity $U_0^* = 2$. The traveling wave $A_2(\omega)$ of wavenumber q_N^* is convectively unstable in region C and absolutely unstable in region A. When $c_3 < 0$ (see enlargement in Fig. 10(b)), the boundary between convective and absolute instability crosses the region where saturated traveling waves are unstable to finite wavelength perturbations but stable to long wave perturbation (for $c_3^l \leq c_3 \leq c_3^r$, between the dashed line and the boundary of the stability region). If we had not considered the stability boundary due to finite wavelength perturbations, we would have obtained inconsistent results since the convective/absolute boundary would have crossed the stability region (that we would have interpreted to extend up to the dashed line in Fig. 10).

We have followed the same protocol to plot in Fig. 11 the convective instability boundaries of traveling waves $A_2(\omega)$ for different rescaled velocities $U_0^* \equiv U_0 \mu^{-1/2}$. As before, we plot the reduced wavenumber $q_N^* \equiv q_N \mu^{-1/2}$ as a function of c_3, for $c_1 = 3$. U_0^* takes values from $U_0^* = 0$ to 4 with a step of 0.4). For each rescaled advection

velocity, the boundary between convective and absolute instability is made up of lines bounding tongues in which the traveling wave corresponding to the rescaled wavenumber q_N^* is convectively unstable (C). For $U_0^* = 0$ the tongues are symmetric in $q_N^* \to -q_N^*$ due to the $x \to -x$ symmetry of the problem and have been obtained by Weber et al. [64] and Aranson et al. [32]. When U_0^* is non-zero, the tongues are no longer symmetric and negative wavenumbers must be considered separately. Note that for $q_N^* > 0$ ($q_N^* < 0$), the size of the convective region decreases (increases) when the advection velocity is increased. When $c_3^l \leq c_3 \leq c_3^r$ and for each velocity U_0^* smaller than a critical value (between 3.6 and 4.0), the corresponding boundary between the convective and absolute region crosses the dashed line in Figs. 11(a,b), and therefore enters the region where traveling waves are unstable but stable to long wave perturbations. This result is consistent when the neutral Eckhaus wavenumber due to finite wavelength perturbations is considered (Eq. (B.2)). Figures such as Fig. 11 should be computed for every value of c_1.

4.3.3. Secondary instability of an NG mode varying the control parameter

We can now test the conjecture that the global secondary bifurcation coincides with the local absolute instability of the traveling wave which represents the 'wing' of the NG mode.

To compare the secondary global bifurcation of the flow with the secondary absolute instability of the wing of the NG mode, we fix c_3 (in the following examples, $c_3 = 1.5$), and U_0^* is decreased from its value at the primary bifurcation threshold till the second bifurcation is obtained. For each value U_0^*, we perform a simulation of the partial differential equation (1) and when the amplitude of the system has reached a steady state, the wavenumber of the wing of the corresponding NG mode is measured and plotted in Fig. 11. The star, the cross and the circle in Fig. 11(c) constitute three examples of such numerical experiments, for advection velocities $U_0^* = 2$ (star), $U_0^* = 1.6$ (cross) and $U_0^* = 1.2$ (circle). For each of these velocities, the domain of absolute instability has been computed in Fig. 11.

Fig. 12 shows spatiotemporal plots of the amplitude resulting from simulations of the partial differential Eq. (1) for two typical cases described above: $U_0^* = 1.6$ and $U_0^* = 1.2$. The amplitude $|A|$ is plotted in grayscale with zero values corresponding to black and maximum amplitude to white. When $U_0^* = 1.6$ (Fig. 12(a)), the amplitude grows from the uniform initial state $A = 0$. Secondary perturbations develop an oscillation in the amplitude as shown by the inclined lines in the lower right part, but they are advected as the simulation proceeds and ultimately leaves the medium. Since parameters are far from the primary bifurcation threshold, the growth length of the solution is small as shown by the small black band near $x = 0$ (corresponding to a small amplitude region). The transient dies out and the long-time asymptotic state of the system is an NG mode as shown by the upper part of the plot which is black near $x = 0$ and uniformly gray in the upper right part. The wavenumber of its wing is measured and plotted as the cross in Fig. 11(c). We verify that it belongs to the convective instability tongue of the wing corresponding to $U_0^* = 1.6$. This result seems to be generic. In each simulation we have performed, for which a stable NG mode is reached, the wavenumber of its wing, when properly rescaled, belongs to a convective instability tongue for the corresponding rescaled advection velocity U_0^*. For example, the star in Fig. 11 represents similar results for $U_0^* = 2$, and indeed, the corresponding value of q_N^* (the star in Fig. 11(c)) belongs to the convectively unstable domain for $U_0^* = 2$.

By contrast, for $U_0^* = 1.2$ (Fig. 12(b)), the NG mode is unstable. The solution starts to grow spatially as an NG mode, but it neither reaches a traveling wave at $x \to +\infty$, nor becomes time periodic. A disordered regime eventually appears with defects where the amplitude is zero at some point. This is indicated by the greater contrast between the maxima of the amplitude, which reaches higher values than below the secondary bifurcation (white thin lines), and the minima which reach zero values (large black bands in the right part of Fig. 12(b)). This regime resembles the defect turbulence observed by Chaté and Manneville [50] among others. But it remains to be determined if the transition to disorder possesses a single step or if multiperiodic states and chaotic régime are obtained via successive global bifurcations.
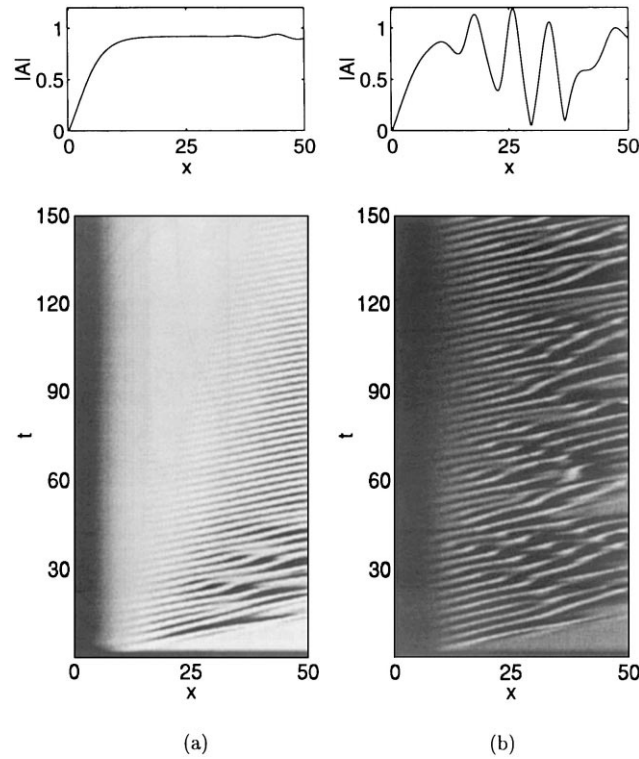
Fig. 12. Spatio-temporal diagram of the evolution of the amplitude in gray scale. $|A| = 0$ corresponds to black. The upper plots show $|A|$ as a function of x at $t = 150$. (a) Simulation for $c_1 = 3$, $c_3 = 1.5$, $U_0^* = 1.6$ (cross in Fig. 11. An NG mode is obtained and parameters are in the convective instability tongue of the wing corresponding to $U_0^* = 1.6$. (b) Simulation above the secondary bifurcation for $c_1 = 3$, $c_3 = 1.5$, $U_0^* = 1.2$. No NG mode is obtained. The system does not evolve to a time-periodic state. Defects continuously appear and the nature (multiperiodic or chaotic) of this global secondary transition has yet to be determined.

Our hypothesis of a secondary bifurcation given by the absolute instability of the wing is confirmed since the wavenumber measured in each globally stable case ($U_0^* = 2$ and $U_0^* = 1.6$) belongs to the corresponding convective instability tongue of the wing. When the flow is (secondarily) globally unstable (for $U_0^* = 1.2$, circle in Fig. 11), it is not possible to determine the wavenumber of the wing from numerical simulation of the partial differential equation (1), because the system evolves towards a solution which is not asymptotic to a traveling wave in the wing. Instead, the wavenumber has been evaluated from the the solution of the dynamical system (11)–(13), using the nonlinear frequency selection criterion of Section 2.3, and it has been checked that the frequency obtained from this criterion is the oscillation frequency measured close to the origin. This value of q_N^* belongs to the absolute domain of Fig. 11 (curve for $U_0^* = 1.2$).

To conclude this section, there is numerical evidence that the absolute instability of the wing of an NG mode determines the stability of the NG mode. It would be interesting to perform a full linear instability analysis of the NG modes involving their entire spatial structure, in order to confirm this conjecture or, in contrast, to determine if a core instability as in the case of the Nozaki–Bekki hole [30] may occur, at least in some range of the (c_1, c_3) plane.

4.3.4. Stability of the NG modes at threshold $\mu = \mu_A$

The preceding analysis for arbitrary μ can be specialized to the NG threshold μ_A. Since the wing of the NG mode at the NG threshold is analytically determined, we are now able to determine if this traveling wave is stable,
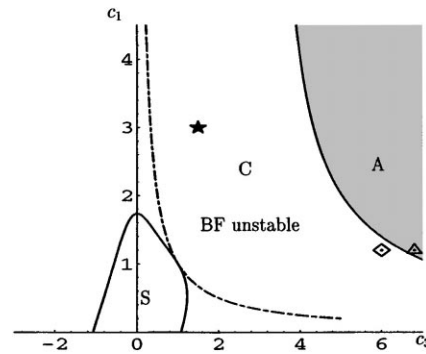
Fig. 13. Regions of linear stability (S), convective (C) instability and absolute (A) instability of the 'wing' $A_2(\omega_A)$ of the NG mode at the NG threshold. In the region (S) (in white), $A_2(\omega_A)$ is linearly stable. The 'wing' of the NG mode is convectively unstable at the NG threshold in the light gray region. The NG mode at the threshold μ_A is absolutely unstable to the right of the solid line (dark gray region). The right of the dashed-dotted line defines the Benjamin–Feir unstable region $1 - c_1 c_3 < 0$. The points represent parameter values used in the simulations presented in Fig. 12 (star), Fig. 14(a) (diamond), and Fig. 14(b) (triangle).

convectively or absolutely unstable. We then explore numerically the relation between this result and the stability of the corresponding NG mode. When the parameters U_0, c_1, c_3 are fixed, the threshold of NG instability is $\mu_A = U_0^2/4(1 + c_1^2)$ and the NG mode (and therefore its wing) oscillates at the frequency $\omega_G(\mu_A) = \omega_A = -c_1 \mu_A$. The corresponding wave number at $x \to +\infty$ (in the wing part) $q_N(\omega_A)$ is then a function of U_0, c_1, c_3, but the rescaled wavenumber $q_A^* \equiv q_N(\omega_A)/\sqrt{\mu_A}$ is a function only of c_1 and c_3.

$$q_A^* = \frac{(1 + c_3^2)^{1/2} - (1 + c_1^2)^{1/2}}{c_1 + c_3}. \tag{37}$$

By testing whether q_A^* is in the Eckhaus stable band, we have obtained the region in the (c_1, c_3) plane in which the traveling wave $A_2(\omega_A)$ is linearly stable. Fig. 13 shows this region plotted in white and labeled by the S symbol. The loss of stability of the saturated traveling wave q_A^*, determined by the intersection of q_A^* and $q_E^*(c_1, c_3)$, turns out to be always due to long-wave perturbation. All numerical simulations of the evolution equation (1) performed in this region show that the system indeed evolves to a stable NG mode. But stable NG modes have been also obtained when parameters are chosen outside of this region of linear stability.

Note that even in the Benjamin–Feir unstable domain (BF region delimited by the dashed curve), an NG mode may be obtained as the ultimate state of the system. This will be shown in Fig. 14(a), where we present the results of simulating partial differential equation (1) for the parameters indicated by the diamond in Fig. 13.

We have determined the region of parameter space for which the saturated traveling wave $A_2(\omega_A)$ at the global threshold is convectively unstable. Results are plotted in Fig. 13: the region of convective instability is plotted in light gray and absolute instability in dark gray.

The simulations in Fig. 14 reported in the form of spatiotemporal plots of the amplitude in gray level from zero (dark) to high values (white) have been undertaken for parameter values indicated in Fig. 13, corresponding to $c_3 = 6.0$ (diamond) or $c_3 = 6.8$ (triangle) with $c_1 = 1.2$. For these simulations, we have chosen $\mu = 1$ and U_0 is 5% below the value corresponding to the NG threshold. The system, initially in the uniform state $A = 0$, (dark zone in the lower part of the diagram) evolves rapidly to an NG mode with a large growth length as indicated by the black part near the origin in Fig. 14(a). This is due to the fact that parameters are close to the primary bifurcation threshold. Fig. 14(a) corresponds to the diamond point in Fig. 13. It belongs to the convectively unstable region of the wing (light gray region in Fig. 13) and we see in Fig. 14(a) that a stable global mode is reached at large time. The transient is long-lived, but is finally advected away. In the region where the amplitude has reached its
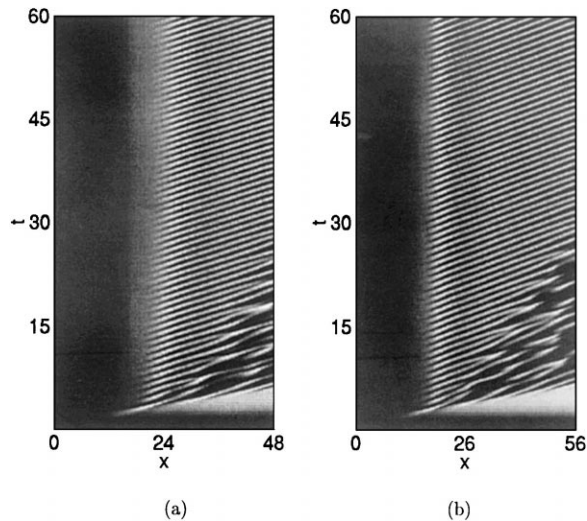
Fig. 14. Same as Fig. 12. (a) Simulation for the parameters indicated by the diamond in Fig. 13 ($c_1 = 1.2$, $c_3 = 6$) and $\mu = 1$, U_0 is 5% below the value corresponding to the NG instability threshold. Ultimately, a pure NG mode is obtained (the transient being washed downstream) as expected given the convective instability of the wing. (b) Simulation for the parameters indicated by the triangle in Fig. 13 ($c_1 = 1.2$, $c_3 = 6.8$) and identical values for μ and U_0. No NG mode is obtained as the transient does not die out since the absolute instability threshold of the wing has been exceeded.

saturation value, perturbations are amplified and develop a spatial oscillation of the amplitude $|A|$, but they are advected downstream as indicated by the inclined lines representing the motion of amplitude maxima on the right of Fig. 14(a). Ultimately, the system evolves to the stable NG mode. Transients leave the medium slowly because parameters are close to the boundary of secondary global instability. The triangle in Fig. 13 represents a set of parameters (c_1, c_3) chosen in the dark gray region when the secondary instability of the wing of the NG mode at threshold is absolute. In that case, the system never evolves to a stable NG mode as demonstrated by the numerical simulation reported in Fig. 14(b). The upstream part of the solution grows as a NG mode (black region near the origin) but at some location in the saturated region (gray), the amplitude starts to oscillate around its saturation value and never reaches a steady state, as indicated by the inclined lines which contaminate the right part of Fig. 14(b). In this case, as soon as the flow is primarily globally unstable, it is also secondarily globally unstable and a complex solution bifurcates at the primary threshold.

In conclusion, let us summarize the two scenarios obtained for the transition to disorder. In the white and light gray regions in Fig. 13, the scenario for the transition to disorder consists of a sequence of bifurcations, with a secondary bifurcation threshold greater than that of the primary bifurcation. We have indeed presented simulations of the evolution Eq. (1) which are in agreement with this scenario: the star in Fig. 13 is plotted for the parameters values used in the simulations presented in Fig. 12. For the values $c_1 = 3$, $c_3 = 1.5$ chosen in Fig. 12, the NG mode obtained at the threshold μ_A is stable and its wing is indeed convectively unstable since the associated point on Fig. 13 (the star) is in the convective region (in light gray). This is the reason why we have obtained a sequence of bifurcations. It is now clear that a condition for obtaining this sequence is that the saturated wave of rescaled wavenumber q_A^* at threshold must be convectively unstable or stable. By contrast, another scenario occurs if c_1 and c_3 are such that $A_2(\omega_A)$ is absolutely unstable, i.e. in the dark gray region in Fig. 13; an intricated dynamics is obtained at the primary global bifurcation μ_A. In the latter case, the route to disorder may possess a single step.

Such simulations indicate that the transition to disorder consists of a sequence of bifurcations when the wing of the NG mode obtained above the primary bifurcation is convectively unstable or stable; the secondary global instability threshold coincides with the threshold of absolute instability of the wing. A direct transition to disorder is obtained

when the wing of the NG mode at threshold is already absolutely unstable. In the latter case, the secondary global instability threshold coincides with the primary instability threshold, i.e. with the absolute instability threshold of the basic state $A = 0$.

5. Conclusions

We have described the NG modes for the one-dimensional Ginzburg–Landau equation. NG modes consist of time oscillating solutions linking the state $A = 0$ (the boundary condition) to a saturated state represented by a traveling wave. We have shown that NG modes exist when the bifurcation parameter exceeds a critical value corresponding to the absolute/convective instability threshold of the basic state $A = 0$. We have proposed a frequency selection criterion for the NG modes relying only on numerical computation in phase space, which actually represents the existence condition of an NG mode. Our criterion has been validated by numerical simulations of the evolution equation (1). We have derived scaling laws for the frequency, the growth length and the slope at the origin of NG modes as functions of the departure from the NG threshold. These scaling laws, derived analytically for the first time, explain the power law obtained numerically by simulation of Navier–Stokes equations for the NG modes in the Taylor–Couette problem with throughflow by Büchel et al. [11] and for Rayleigh–Bénard convection with an added Poiseuille flow by Müller et al. [12,13]. We have addressed the question of the domain of parameter space in which an NG mode is stable. We have therefore studied the convective/absolute nature of the instability of the traveling wave to which an NG mode is asymptotic when $x \rightarrow +\infty$ (called the wing). We have conjectured that the loss of stability of an NG mode is due to the change of nature of the instability (from convective to absolute) of its wing. This conjecture has been tested by determining the absolute/convective instability of traveling waves. Numerical temporal simulations in the globally unstable region are found to agree with this hypothesis. A nonperiodic solution with continually generated defects is obtained when the bifurcation parameter is increased above the secondary global bifurcation threshold. The nature of this global secondary transition remains to be determined. We have shown that the primary and the secondary instability may occur in sequence when varying a control parameter. The transition to disorder occurs in one step right at the primary global instability threshold whenever the NG mode is unstable above the primary instability threshold. At the NG threshold, direct numerical simulations indicate that convective instability of the wing corresponds to instability of the NG modes. When the wing of an NG mode at threshold μ_A is already absolutely unstable, the bifurcated solution of the flow cannot be an NG mode; the only possible self-sustained solution to which the system inevitably evolves, is a more complicated, aperiodic solution.

Acknowledgements

Appendix A. Details of the inner and outer solutions

A.1. Outer solution

By setting the bifurcation parameter value to $\mu = \mu_A + \epsilon$ and the frequency to $\omega_A + \epsilon\,\omega_1$ with $\epsilon \ll 1$, and ω_1 to be determined, the outer solution of Eqs. (22)–(24), representing the stable manifold of $A_2(\omega)$ just above the

threshold and away from the origin, is sought in the form of perturbed series:

$$u_o(a) = \frac{da}{dx} = \sum_{j=0}^{+\infty}(v_j + \epsilon\lambda_j)(a_N - a)^j, \tag{A.1}$$

$$q_o(a) = \sum_{j=0}^{+\infty}(\rho_j + \epsilon\eta_j)(a_N - a)^j. \tag{A.2}$$

At the threshold ($\epsilon = 0$), the coefficients v_j, ρ_j are those of the heteroclinic orbit $q_f(a)$, $u_f(a)$ corresponding to the Kolmogorov front solution [43] and are computed recursively and numerically. The coefficients λ_j, η_j are assumed to be linear functions of ω_1 i.e. $\lambda_j = \lambda_j^0 + \omega_1\lambda_j^1$, $\eta_j = \eta_j^0 + \omega_1\eta_j^1$ and represent the departure of the NG mode from the front solution. They are recursively and numerically computed in the same manner as v_j and ρ_j by requiring that Eqs. (A.1) and (A.2) satisfy Eqs. (22)–(24) at each order in ϵ and j, and for each value of ω_1. To start the recurrence, we need to use the boundary condition at $x \to +\infty$ which reads

$$u_o(a_N(\mu_A + \epsilon, \omega_A + \epsilon\omega_1)) = 0, \tag{A.3}$$

$$q_o(a_N(\mu_A + \epsilon, \omega_A + \epsilon\omega_1)) = q_N(\mu_A + \epsilon, \omega_A + \epsilon\omega_1). \tag{A.4}$$

For the outer solution, the boundary condition at $+\infty$ yields the leading order coefficients for u_0 and q_0 series: $v_0 = 0$, $\rho_0 = q_N(\omega_A)$, and at first order the equations (also given by Eqs. (23) and (24) at first order)

$$2(q_N - q_0)v_1 - c_0U_0\rho_1 - v_1\rho_1 - 2I_3a_N^2 = 0, \tag{A.5}$$

$$c_0U_0v_1 + 2(q_N - q_0)\rho_1 - v_1^2 + 2R_3a_N^2 = 0. \tag{A.6}$$

Eqs. (A.5) and (A.6) give us v_1 and ρ_1 by elimination of ρ_1:

$$v_1^3 + 4k_0v_1^2 + (4(q_N - q_0)^2 + 4k_0^2 - 2R_3a_N^2)v_1 - 4(q_N - q_0)I_3a_N^2 - 4R_3a_N^2k_0 = 0. \tag{A.7}$$

The positive root of equation (A.7) determines v_1 which is unique as required by the condition that the front solution be unique. Once v_1 and ρ_1 are determined, λ_0 and η_0 are computed by equations

$$(2(q_N - q_0) - \rho_1)\lambda_0 - c_0U_0\eta_0 = c_0(c_1 - \omega_1) \tag{A.8}$$

$$c_0U_0\lambda_0 + (2(q_N - q_0) - v_1)\lambda_0 = c_0(1 + c_1\omega_1) \tag{A.9}$$

which may be split into two parts according to the linear dependence of λ_0 and η_0 as functions of ω_1. Then all coefficients (v_j, ρ_j), (λ_j, η_j) are computed recursively, each pair being the solution of a linear system of equations for which the r.h.s. depends only on coefficients with smaller index. Once all coefficients have been computed, we obtain the asymptotic behaviour of the outer solution close to the origin where the inner solution prevails,

$$u_o(a) \stackrel{a\to 0}{\simeq} \sum_{j=0}^{+\infty}v_ja_N^j - a\sum_{j=0}^{+\infty}jv_ja_N^{j-1} + \epsilon\sum_{j=0}^{+\infty}\lambda_ja_N^j, \tag{A.10}$$

$$q_o(a) \stackrel{a\to 0}{\simeq} \sum_{j=0}^{+\infty}\rho_ja_N^j - a\sum_{j=0}^{+\infty}j\rho_ja_N^{j-1} + \epsilon\sum_{j=0}^{+\infty}\eta_ja_N^j. \tag{A.11}$$

Obviously $u_o(a)$ and $q_o(a)$ given by Eqs. (A.10) and (A.11) cannot satisfy the boundary condition at $a = 0$.

A.2. Inner solution

To satisfy the boundary condition at the origin, we introduce an inner layer near $a = 0$ where the amplitude $a(x)$ of the inner solution remains small. Using the variable ξ such that $a = |A| = \theta(\epsilon)\xi$, where $\theta(\epsilon)$ denotes the size in amplitude of the inner layer, we linearize the dynamical system (22)–(24) around $a = 0$ and seek a solution of the linearized system satisfying the boundary condition $\xi(0) = 0$. All the bounded trajectories already described in Section 2 which exist in the plane $a = 0$ and link A_0^- to A_0^+ [39] cannot be considered as valid inner solutions to find an NG mode since they do not depart from the plane $a = 0$ with a finite slope at the origin. By contrast, the separatrices Eqs. (18) and (19) which possess a singularity (infinite k when $x = 0$) are the only solutions departing from the plane $a = 0$ with a finite slope $u = \dot{a}$ at the origin and therefore will constitute the inner solution of the problem. Solutions (18),(19) and (21) are rewritten using $\mu = \mu_A + \epsilon$ and $\omega = \omega_A + \epsilon$, after rescaling the previously introduced coefficients α and β representing the departures of the wavenumber q from q_0 and spatial growth rate k from k_0 at A_0^- : $\alpha = \alpha_1 \epsilon^{1/2}$ and $\beta = \beta_1 \epsilon^{1/2}$;

$$\xi = v_0 (2|\zeta_1|)^{-1/2} e^{k_0 x} \left(\cosh(2\alpha_1 \epsilon^{1/2} x) - \cos(2\beta_1 \epsilon^{1/2} x) \right)^{1/2}, \tag{A.12}$$

$$q_i = q_0 + \epsilon^{1/2} \frac{\beta_1 \sinh(2\alpha_1 \epsilon^{1/2} x) - \alpha_1 \sin(2\beta_1 \epsilon^{1/2} x)}{\cosh(2\alpha_1 \epsilon^{1/2} x) - \cos(2\beta_1 \epsilon^{1/2} x)}, \tag{A.13}$$

$$k_i = k_0 + \epsilon^{1/2} \frac{\alpha_1 \sinh(2\alpha_1 \epsilon^{1/2} x) + \beta_1 \sin(2\beta_1 \epsilon^{1/2} x)}{\cosh(2\alpha_1 \epsilon^{1/2} x) - \cos(2\beta_1 \epsilon^{1/2} x)}, \tag{A.14}$$

with $|\zeta_1| = (c_0(1 + \omega_1^2))^{1/2}$, $\alpha_1 = ((|\zeta_1| - \kappa_1)/2)^{1/2}$, $\beta_1 = ((|\zeta_1| + \kappa_1)/2)^{1/2}$, and $\kappa_1 = c_0(1 + c_1\omega_1)$. The $\epsilon^{1/2}$ rescaling comes from the beating of the two waves associated with A_0^+ and A_0^-. Solution (A.12) indeed satisfies the boundary condition $\xi(0) = 0$. When $x \to +\infty$, we seek the asymptotic behaviour of the inner solution $\xi(x)$, $k_i + iq_i$ in order to match with the outer solutions (A.10) and (A.11). The maximum of the function $\xi(x)$ may be obtained for a value close to $x = \pi\epsilon^{-1/2}/\beta_1$ and the matching must be done close to this value. Therefore, the asymptotic behaviour of the inner solution reads when $x \sim \pi\epsilon^{-1/2}/\beta_1$,

$$\xi(x) \simeq v_0 (2|\zeta_1|\epsilon)^{-1/2} e^{k_0 \pi \epsilon^{-1/2}/\beta_1} \left(\cosh\left(\frac{2\alpha_1 \pi}{\beta_1} \right) - 1 \right)^{1/2}, \tag{A.15}$$

$$k_i + iq_i \simeq k_0 + iq_0 + \epsilon^{1/2}(\alpha_1 + i\beta_1) \frac{\sinh(2\alpha_1 \pi/\beta_1)}{\cosh(2\alpha_1 \pi/\beta_1) - 1}. \tag{A.16}$$

Appendix B. Neutral Eckhaus wavenumber when the loss of stability is due to finite wavelength perturbations

When only long-wave perturbations are considered, the stability of saturated traveling waves of type Eq. (4) is determined by the Eckhaus wavenumber q_E^* given by Eq. (34). Any traveling wave of wavenumber q_N^* with $q_N^{*2} > q_E^{*2}$ is unstable for long-wave perturbations. Matkowsky and Volpert [36] have shown that the saturated traveling waves of type Eq. (4) are also unstable for finite wavelength perturbations in the region of the plane (c_1, c_3) above (with $c_1 > 0$) the curve of equation:

$$c_1 = -\frac{1}{c_3} \quad \text{if} \quad c_3^2 < \frac{1}{3}$$

$$c_1 = \frac{-2c_3(c_3^2 - 1) + \sqrt{4c_3^2(c_3^2 - 1)^2 + (3c_3^2 - 1)(5c_3^2 + 1)}}{3c_3^2 - 1} \quad \text{if} \quad c_3^2 > \frac{1}{3}, \tag{B.1}$$

The neutral Eckhaus wavenumber for which the saturated traveling waves of type Eq. (4) become unstable to finite wavelength perturbations is no longer given by Eq. (34) but reads in this case:

$$q_E^{*2} = \frac{A}{1 + A} \tag{B.2}$$

where A is given in terms of several intermediate functions written below,

$$A = \frac{3p_y^2 + 4p_y + 1 - 4\xi(p_y + 1)}{8(p_y - \xi)},$$

$$p_y = (-q + \sqrt{\delta})^{1/3} + (-q - \sqrt{\delta})^{1/3} + \frac{4\xi + 1}{3},$$

$$q = B^3 + \eta, \qquad \delta = p^3 + q^2, \qquad p = \eta - B^2,$$

$$B = \frac{2\xi - 1}{3}, \qquad \eta = \frac{1 + c_3^2}{1 + c_1^2}, \qquad \xi = -\frac{1 - c_1 c_3}{1 + c_1^2}.$$

References

[1] M.C. Cross, P.C. Hohenberg, Pattern formation outside of equilibrium, Rev. Mod. Phys. 65 (1993) 851–1112.
[2] P. Huerre, P.A. Monkewitz, Local and global instabilities in spatially developing flows, Annu. Rev. Fluid Mech. 22 (1990) 473–537.
[3] A. Couairon, J.-M. Chomaz, Global instability in nonlinear systems, Phys. Rev. Lett. 77 (1996) 4015–4018.
[4] A. Couairon, J.-M. Chomaz, Absolute and convective instabilities, front velocities and global modes in nonlinear systems, Physica D 108 (1997) 236–276.
[5] A. Couairon, J.-M. Chomaz, Pattern selection in the presence of a cross flow, Phys. Rev. Lett. 79 (14) (1997) 2666-2669.
[6] C. Mathis, M. Provansal, L. Boyer, The Bénard von Kármán instability: an experimental study near the threshold, J. Phys. (Paris) Lett. 45 (1984) 483.
[7] S. Goujon-Durand, P. Jenffer, J.E. Wesfreid, Downstream evolution of the Bénard-von Kármán instability, Phys. Rev. E 50 (1994) 308.
[8] B.J.A. Zielinska, J.E. Wesfreid, On the spatial structure of global modes in wake flow, Phys. Fluids 7(6) (1995) 1418–1424.
[9] J.E. Wesfreid, S. Goujon-Durand, B.J.A. Zielinska, Global mode behavior of the streamwise velocity in wakes, J. Phys. II France 6 (1996) 1–14.
[10] A. Couairon, J.-M. Chomaz, Fully nonlinear global modes in slowly varying flows, Phys. Fluids, 1998, submitted for publication.
[11] P. Büchel, M. Lücke, D. Roth, R. Schmitz, Pattern selection in the absolutely unstable regime as a nonlinear eigenvalue problem: Taylor vortices in axial flow, Phys. Rev. E 53 (1996) 4764–4777.
[12] H.W. Müller, M. Lücke, M. Kamps, Convective patterns in horizontal flow, Europhys. Lett. 10 (1989) 451–456.
[13] H.W. Müller, M. Lücke, M. Kamps, Transversal convection patterns in horizontal shear flow, Phys. Rev. A 45 (1992) 3714–3726.
[14] S. Tobias, M.R.E. Proctor, E. Knobloch, Convective and absolute instabilities of fluid flows in finite geometries, Physica D 113 (1998) 43.
[15] W. van Saarloos, P.C. Hohenberg, Fronts, pulses, sources and sinks in generalized complex Ginzburg–Landau equations, Physica D 56 (1992) 303–367.
[16] P. Kolodner, J.A. Glazier, Interaction of localized pulses of traveling-wave convection with propagating disturbances, Phys. Rev. A 42 (1990) 7504.
[17] G. Ahlers, D.S. Cannel, Vortex-front propagation in rotating Couette–Taylor flow, Phys. Rev. Lett. 50 (1983) 1583–1586.
[18] A. Hanna, A. Saul, K. Showalter, Detailed studies of propagating fronts in the iodate oxidation of arsenous acid, J. Am. Chem. Soc. 104 (1982) 3838.
[19] J.V. Moloney, A.C. Newell, Nonlinear optics, Physica D 44 (1990) 1–37.
[20] P.A. Bélanger, L. Gagnon, C. Paré, Solitary pulses in an amplified nonlinear dispersive medium, Opt. Lett. 14 (1989) 943.
[21] H. Chaté, Spatio-temporal intermittency regimes of the one-dimensional complex Ginzburg–Landau equation, Nonlinearity 7 (1994) 185.
[22] A. Pumir, B.I. Shraiman, W. van Saarloos, P.C. Hohenberg, H. Chaté, M. Holen, Phase vs. defect turbulence in the 1-d complex Ginzburg–Landau equation, in: C.D. Andereck, F. Hayot (Eds.), Ordered and Turbulent Patterns in Taylor–Couette flow, Plenum Press, New York, 1992.

[23] L. Gil, Space and time intermittency behavior of a 1-d complex Ginzburg–Landau equation, Nonlinearity 4 (1991) 1213.

[24] M. van Hecke, Building blocks of spatiotemporal intermittency, Phys. Rev. Lett. 80 (1997) 1896–1899.

[25] J. Fineberg, V. Steinberg, Vortex-front propagation in Rayleigh–Bénard convection, Phys. Rev. Lett. 58 (1987) 1332–1335.

[26] A.C. Newell, J.A. Whitehead, Finite bandwidth, finite amplitude convection, J. Fluid Mech. 38 (1969) 279.

[27] L.A. Segel, Distance side-walls cause slow amplitude modulation of cellular convection, J. Fluid Mech. 38 (1969) 203.

[28] K. Stewartson, J.T. Stuart, A nonlinear instability theory for a wave system in plane Poiseuille flow, J. Fluid Mech. 48 (1971) 529.

[29] H. Sakaguchi, Instability of the hole solution in the complex Ginzburg–Landau equation, Prog. Theor. Phys. 85 (1991) 417–421.

[30] H. Chaté, P. Manneville, Stability of the Bekki–Nozaki hole solutions to the one-dimensional complex Ginzburg–Landau equation, Phys. Lett. A 171 (1992) 183–188.

[31] S. Popp, O. Stiller, I. Aranson, L. Kramer, Hole solutions in the 1D complex Ginzburg–Landau equation, Physica D 84 (1995) 398–423.

[32] I.S. Aranson, L. Aranson, L. Kramer, A. Weber, Stability limits of spirals and traveling waves in nonequilibrium media, Phys. Rev. A 46 (1992) R2992-R2995.

[33] R.J. Briggs, Electron-Stream Interaction with Plasmas, MIT Press, Cambridge, MA, 1964.

[34] A. Bers, Space time evolution of plasma instabilities – absolute and convective, in: M.N. Rosenbluth, R.Z. Sagdeev (Eds.), Handbook of Plasma Physics, North-Holland, Amsterdam, 1983, pp. 451–517.

[35] E.M. Lifshitz, L.P. Pitaevskii, Physical Kinetics, Pergamon, London, 1981.

[36] B.J. Matkowsky, V. Volpert, Stability of plane wave solutions of complex Ginzburg–Landau equations, Quart. Appl. Math. 51 (1993) 265–281.

[37] J.-M. Chomaz, P. Huerre, L.G. Redekopp, The effect of nonlinearity and forcing on global modes, In: P. Coullet, P. Huerre (Eds.), New trends in Nonlinear Dynamics and Pattern-forming Phenomena, Plenum Press, New York, 1990, pp. 227–240.

[38] J.-M. Chomaz, P. Huerre, L.G. Redekopp, Models of hydrodynamic resonances in separated shear flows, in: Proc. 6th Symp. on Turbulent Shear Flows, Toulouse, France, 1987, pp. 321–326.

[39] M.J. Landman, Solutions of the Ginzburg–Landau equation of interest in shear flow transition, Stud. Appl. Math. 76 (1987) 187.

[40] J.A. Powell, C.K.R.T. Jones, T.M. Kapitula, Nearly real fronts in a Ginzburg–Landau equation, Proc. R. Soc. Edinburgh 116A (1990) 193.

[41] N. Koppel, L.N. Howard, Plane wave solutions to reaction–diffusion equations, Stud. Appl. Math. 56 (1973) 291.

[42] V.I. Arnol'd, Geometrical Methods in the Theory of Ordinary Differential Equations, Springer, Heidelberg, 1983.

[43] A. Kolmogorov, I. Petrovsky, N. Piskunov, Investigation of a diffusion equation connected to the growth of materials, and application to a problem in biology, Bull. Univ. Moscow, Ser. Int. Sec. A 1 (1937) 1.

[44] A.C. Newell, T. Passot, J. Lega, Order parameter equations for patterns, Annu. Rev. Fluid Mech. 25 (1993) 399–453.

[45] W. van Saarloos, Front propagation into unstable states: marginal stability as a dynamical mechanism for velocity selection, Phys. Rev A 37 (1988) 211.

[46] W. van Saarloos, Front propagation into unstable states: II linear versus nonlinear marginal stability and rate of convergence, Phys. Rev A 39 (1989) 6367.

[47] C.M. Bender, S.A. Orszag, Advanced Mathematical Methods for Scientists and Engineers, McGraw-Hill, New York, 1978.

[48] E. Brunet, B. Derrida, Shift in the velocity of a front due to a cutoff, Phys. Rev. E 56 (1997) 2597–2604.

[49] U. Ebert, W. van Saarloos, Universal algebraic relaxation of fronts propagating into an unstable state and implications for moving boundary approximations, Phys. Rev. Lett. 80 (1998) 1650–1653.

[50] H. Chaté, P. Manneville, Phase diagram of the two-dimensional complex Ginzburg–Landau equation, Physica A 224 (1996) 348–368.

[51] W.H. Press, S.A. Teukolsky, W.T. Vetterling, B.P. Flannery, Numerical recipes in fortran, Cambridge University Press, Cambridge, 1994.

[52] C. Cossu, T. Loiseleux, On the convective and absolute nature of instabilities in finite difference numerical simulations of open flows, J. Comput. Phys. 144 (1998) 98–108.

[53] A. Recktenwald, M. Lücke, H.W. Müller, Taylor vortex formation in axial through-flow: linear and weakly nonlinear analysis, Phys. Rev. E 48 (1993) 4444–4454.

[54] L.S. Tuckerman, D. Barkley, Bifurcation analysis of the Eckhaus instability, Physica D 46 (1990) 57–86.

[55] L.S. Tuckerman, D. Barkley, Comment on bifurcation structure and the Eckhaus instability, Phys. Rev. Lett. 67 (1991) 1051–1054.

[56] J.-M. Chomaz, A. Couairon, Against the wind, Phys. Fluids, 1998, submitted for publication.

[57] K. Nozaki, N. Bekki, Exact solutions of the generalized Ginzburg–Landau equation, J. Phys. Soc. Jpn. 53 (1984) 1581–1582.

[58] J. Lega, S. Fauve, Traveling hole solutions to the complex Ginzburg–Landau equation as perturbations of nonlinear Schrödinger dark solitons, Physica D 102 (1997) 234–252.

[59] H.W. Müller, M. Tveitereid, Absolute and convective nature of the Eckhaus and zigzag instability, Phys. Rev. Lett. 74(9) (1995) 1582–1585.

[60] J.-M. Chomaz, A. Couairon, S. Julien, Absolute and convective nature of the Eckhaus and zigzag instability for an arbitrarily oriented throughflow, Phys. Fluids, 1999, submitted for publication.

[61] P. Brancher, J.-M. Chomaz, Absolute and convective secondary instabilities in spatially periodic shear flows, Phys. Rev. Lett. 78 (1997) 658–661.

[62] P. Huerre, M. Rossi, in: P. Manneville (Ed.), Hydrodynamics and Nonlinear Instabilities, Cambridge University Press, Cambridge, 1998.

[63] L. Brevdo, T.J. Bridges, Absolute and convective instabilities of spatially periodic flows, Phil. Trans. R. Soc. London, Ser. A 354 (1996) 1027–1064.

[64] A. Weber, L. Kramer, I.S. Aranson, L. Aranson, Stability limits of traveling waves and the transition to spatiotemporal chaos in the complex Ginzburg–Landau equation, Physica D 61 (1992) 279–283.